

The far ultra-violet background

S. R. KULKARNI¹

¹*Owens Valley Radio Observatory 249-17, Caltech
Pasadena, CA 91125, USA*

(Accepted April 20, 2022)

Submitted to PASP

ABSTRACT

The diffuse far-ultraviolet (FUV) background has received considerable attention from astronomers since the 1970's. The initial impetus came from the hope of detecting UV radiation from the hot intergalactic medium. The central importance of the FUV background to the physics (heating and ionization) of the diffuse atomic phases motivated the next generation of experiments. The consensus view is that the diffuse FUV emission at high latitudes has three components: stellar FUV reflected by dust grains (diffuse Galactic light or DGL), FUV from other galaxies and the intergalactic medium (extra-galactic background light or EBL) and a component of unknown origin (and referred to as the “offset” component). During the 1980's, there was some discussion that decaying dark matter particles produced FUV radiation. In this paper I investigate production of FUV photons by conventional sources: line emission from Galactic Hot Ionized Medium, two-photon emission from the Galactic Warm Ionized Medium and low-velocity shocks, and Lyman- β fluorescence of hydrogen at several locales in the Solar System (the interplanetary medium, the exosphere and the thermosphere of Earth). I conclude that two thirds and arguably all of the offset component can be explained by the sum of the radiation from the processes listed above.

1. BACKGROUND

The diffuse background in the wavelength range 912–2000 Å is of central importance to the physics of the diffuse atomic phases – the Cold Neutral Medium (CNM) and the Warm Neutral Medium (WNM). Even though historically, the various bands of ultra-violet (UV) were defined by wavelength properties of detectors and mirror coatings, here, following the Galaxy Evolution Explorer mission (*GALEX*), the Far-Ultraviolet (FUV) band covers the wavelength range 1350–1750 Å.

The diffuse FUV radiation, via photo-electric ionization of C I and photo-electric heating of dust particles, heats the two atomic phases mentioned above. The same radiation, via ionization of heavier elements also provides residual ionization to the two atomic phases. FUV photons excite the Lyman and Werner bands of H₂ (Duley & Williams 1980) which result in UV fluorescent line emission and once in ten times leads to dissociations (Jura 1974; Draine & Bertoldi 1996). In the process,

the strength of FUV radiation determines the transition in diffuse clouds between atomic and molecular phases.

In the late sixties it was speculated that the hot intergalactic medium (IGM) would be revealed by diffuse FUV emission (see Kurt & Sunyaev 1970; Paresce & Jakobsen 1980; Henry 1991 for summaries of missions). Separately, during the 1970's, the first pulsar surveys found that pulsars signals were invariably dispersed (see, for example, Manchester & Taylor 1977). During the 1980's, thanks primarily to the work of Ronald J. Reynolds, the same ionized medium was complementarily sensed via H α recombination emission. Together these two approaches established the Warm Ionized Medium (WIM) as a distinct phase of the ISM (see Haffner et al. 2009 for a review).

The filling factor of the WIM, by volume, is estimated to be between 20% and 40% of the Galactic disk. The required large ionizing flux is conventionally attributed to Lyman continuum leaking from OB associations (Reynolds 1990). The observed large vertical scale height, \approx 1 kpc, of the WIM was initially a mystery. This “crisis” led to a resurrection of a hypothesis of decaying dark matter as a major source of ionizing pho-

tons (Stecker 1980; Sciama 1990; more recent references include Kollmeier et al. 2014; Henry et al. 2015). Miller & Cox (1993) and Dove & Shull (1994) provided a conventional explanation based on O stars as the principal source of ionizing radiation, radiative transfer modeling and clustering of star-forming regions, “chimneys” and “channels” while Slavin et al. (2000) made a strong case for (high latitude) ionizing radiation resulting from old supernova remnants.

Two missions, both launched in 2003, greatly advanced the field of diffuse FUV radiation. *GALEX* (Martin et al. 2005) carrying both an FUV and a near-UV (NUV; 1750–2800 Å) wide-field imager, each with a field-of-view (FoV) of over a square degree but with pixel size of only a few arc-seconds, undertook an FUV & NUV sky survey. STSAT-1 carrying the Far-UV Imaging Spectrometer (FIMS¹; Edelstein et al. 2006) aimed to study the Galactic Hot Ionized Medium (HIM) by undertaking spectral (900–1750 Å) imaging of the sky at few arc-minute spatial resolution.

The overall consensus is that much of the diffuse FUV emission is due to reflection of stellar FUV photons by diffuse (“cirrus”) clouds and conveniently traced by IRAS 100 μm band or fluorescence by molecular hydrogen. Together this emission is called as the Diffuse Galactic Light (DGL). However, some diffuse background emission is *not* correlated with cirrus clouds, a fraction of which can be reasonably attributed to collective emission from other galaxies and the intergalactic medium – the so-called Extragalactic Background Light (EBL). There remains some 120–180 CU emission in the FUV band which cannot be attributed to either DGL or EBL and was given the name “offset” component.² Here, CU (“continuum unit”) stands for $\text{photon cm}^{-2} \text{s}^{-1} \text{\AA}^{-1} \text{sr}^{-1}$ with “sr” as a short for steradian. A related unit is “line unit” (LU) which stands for $\text{photon cm}^{-2} \text{s}^{-1} \text{sr}^{-1}$. We take the occasion to introduce “Rayleigh” (R) which is a unit for surface brightness of line emission and routinely used in aeronomy. Numerically, one Rayleigh is $10^6/(4\pi) \text{photon cm}^{-2} \text{s}^{-1} \text{sr}^{-1}$.

Separately, the irreducible background for an UV–IR mission located at or about 1 AU, is due to scattering of solar photons by zodiacal dust. However, the Sun is faint in the FUV. Ergo, the sky is dark in the FUV band. As a result, the FUV band is most attractive for low surface brightness imaging of galaxies (O’Connell

1987). Indeed, it is precisely this advantage of the FUV band that allowed *GALEX* to discover very faint star-forming complexes well beyond the optical disk and with sensitivity better than that provided by ground-based H α imaging (e.g., Barnes et al. 2011).

The purpose of this paper is to investigate all plausible conventional origin(s) for this offset component. In §2 we review the measurements of diffuse high-latitude FUV emission, followed by a summary of the physics of hydrogen two-photon decay (§3). We investigate contribution to the FUV band from line emission from the Galactic HIM, two-photon emission from the Galactic WIM and low-velocity shocks (§4) and from fluorescence of atomic hydrogen by Ly β (§5) in the Solar System: the Interplanetary Medium³ (§6), the Earth’s atmosphere (“thermosphere”; §7) and the exosphere (§8). In §9 we tally the contributions to the diffuse FUV background and conclude that about two thirds (and, within uncertainties, possibly all) of the offset component can be accounted for by these contributions. We conclude in §10.

2. THE DIFFUSE FUV EMISSION

The “Interstellar Radiation Field” (ISRF) is composed of both resolved (bright) stars and diffuse emission (e.g., Chapter 12, Draine 2011). Only the latter component is of interest to this paper. There have been extensive reviews of the diffuse FUV emission (e.g. see Paresce et al. 1980; Henry 1991; Henry et al. 2015). Here we focus on the measurements of the diffuse FUV by *GALEX*. *GALEX* was in low-earth orbit (LEO) with an orbital period of 99 minutes. To minimize airglow, observations were restricted to narrow periods lasting only 25–30 minutes during Earth eclipse (Morrissey et al. 2007). The good angular resolution of *GALEX* allowed for masking out point sources and galaxies.

We refer to two major studies of diffuse FUV carried out with *GALEX*: one led by Jayant Murthy and associates (e.g., Murthy et al. 2010; Henry et al. 2015; Akshaya et al. 2018, 2019) and the other, the PhD thesis of Erika Hamden (Hamden et al. 2013). The conclusions from these studies are largely concordant and briefly are as follows:

1. At mid to high Galactic latitudes, the FUV intensity scales linearly with the IRAS 100 μm intensity up to an intensity of 8 MJy sr^{−1} (e.g., Seon

¹ also sometimes referred to as SPEAR

² DGL is proportional to the column density of dust. However, this linear relation has an offset: radiation even when the dust column is very low – hence the name “offset”.

³ The term IPM has two different connotations in astronomy. In radio astronomy, IPM refers to the solar wind that pervades the solar system out to the heliopause. In planetary studies, the IPM stands for the very local interstellar cloud into which the Solar system is moving.

et al. 2011). This is attributed to reflection of stellar FUV photons from hot stars (primarily located in the Galactic plane) by interstellar dust. The same dust particles, heated by stellar light (including the FUV), radiate at long wavelengths and produce the IRAS 100 μm band, hence the correlation. The FUV emission saturates at higher values of 100 μm emission presumably because the absorption of the FUV radiation by the clouds outweighs over reflection.

2. The FUV intensity increases in the direction of interstellar clouds which harbor molecular hydrogen. This is attributed to fluorescence by photons in the Lyman band (912–1216 \AA) and FUV photons (see Martin et al. 1990; Jo et al. 2017).
3. At high Galactic latitudes, diffuse FUV background is present, even in directions towards dust-free regions. Akshaya et al. (2019) estimate the EBL contribution to be 96–131 CU and partition it as follows: 60–81 CU from other galaxies, 16–30 CU from QSOs and < 20 CU from the IGM (and attribute this estimate to Martin et al. 1991).

Hamden et al. (2013) conclude “*There is a ~ 300 CU FUV isotropic offset which is likely due to a combination of air glow (probably the dominant contributor), a small extragalactic background component including continuum light from unresolved galaxies, and/or a Galactic component not traced by other indicators*”.

Akshaya et al. (2018) state “*We find offsets of 230–290 photon units⁴ in the far-UV... Of this, approximately 120 photon units can be ascribed to dust-scattered light and another 110 photon units to extragalactic radiation. The remaining radiation is, as yet, unidentified and amounts to 120–180 photon units in the far-UV.*”

We end this section by noting that, at times in the literature, the diffuse component under discussion is referred to as “isotropic/offset”. We do not consider the isotropic nature to be firmly established since the primary observation is principally from high latitude regions. The term “offset” accurately describes the method by which the strength of the component has been measured. So we will, for short hand, refer to the component under investigation as the “offset” component.

⁴ The “photon unit” discussed here is the same as CU.

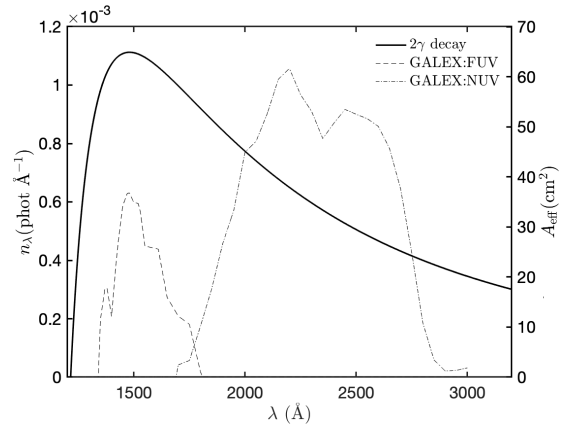


Figure 1. (Left y axis): The photon spectrum of a single two-photon decay, n_λ (solid line) as a function of the wavelength, λ . Since each decay leads to emission of two photons, $\int n_\lambda d\lambda = 2$. (Right y axis): Effective area of *GALEX* FUV and NUV bands as a function of λ (dot-dash and dashed lines). The details of the fitting formula used to generate the two-photon decay spectrum and effective area of *GALEX* can be found in §A.

3. TWO-PHOTON DECAY

An H atom in a 2s level, undisturbed by a collision, will decay by emitting two photons over a timescale of $A_{2\gamma}^{-1} \approx (8.2 \text{ s}^{-1})^{-1}$; see Figure 1. The sum of the energies of the two photons is equal to that of Ly α or 10.2 eV. The factors to convert the two-photon spectrum to FUV and NUV counting rates are central to this paper and a full discussion can be found in §A. The key result is the following: 10^6 two-photon decays $\text{cm}^{-2} \text{ s}^{-1}$ results in 85.1 CU in the FUV channel and 18.4 CU in the NUV channel (Table 3).

4. THE GALAXY

There are three major Galactic sources of diffuse FUV radiation: two-photon continuum from the WIM (recombination) and shocked gas (collisional excitation and recombination) and line emission from the HIM.

4.1. The Warm Ionized Medium

Deharveng et al. (1982) investigated two-photon emission from the WIM and concluded that it could not account for the FUV background. Martin et al. (1991) and Reynolds (1992) and came to similar conclusions. Rather than compute the expected two-photon emission from the physical parameters of the WIM (as was done in the past papers) we prefer the simpler approach of estimating the two-photon brightness directly from observations of H α . At the temperature of the WIM (8,000 K), assuming case B, we expect that for every two-photon decay there are 1.47 H α photons.

In Figure 2 we display the histogram of Galactic H α surface brightness as recorded in the Wisconsin H α Mapper Sky Survey (WHAM-SS or WHAM for short; Haffner et al. 2003, 2010). From these figures we conclude that the Galactic H α emission towards the Galactic polar cap is approximately 0.5 R. We subtract 20% to account for contribution resulting from scattering of H α emission by cirrus clouds (Witt et al. 2010; Dong & Draine 2011). The expected two-photon decay rate is then 0.27 R which corresponds to 23 CU in the FUV band, consistent with the estimate of 18–36 CU (Seon et al. 2011).

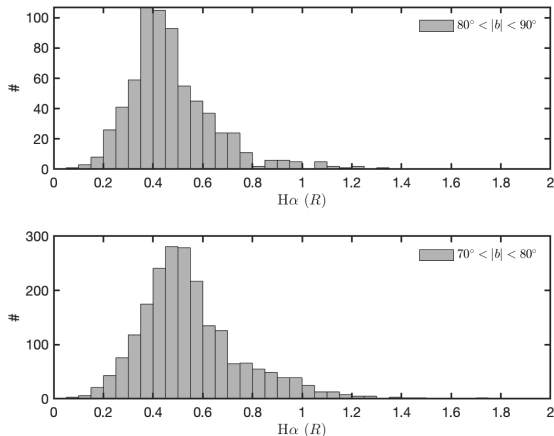


Figure 2. Histogram of the WHAM H α brightness towards the Galactic caps. The vertical-axis refers to the number of WHAM beams. The size of the WHAM beam is about a degree. Data obtained from WHAM (Haffner et al. 2003, 2010)..

4.2. The Hot Ionized Medium

The three dominant metals have strong resonance lines (2s \rightarrow 2p) in the UV, which conveniently probe a range of temperatures (Sutherland & Dopita 1993): CIV ($\lambda\lambda$ 1548.2, 1550.8 Å; 1×10^5 K), NV ($\lambda\lambda$ 1242.8, 1238.8 Å; 2×10^5 K) and OVI ($\lambda\lambda$ 1037.6, 1031.9 Å; 3×10^5 K). FUSE observations of OVI established the presence of widespread HIM in the halo of the Galaxy (Savage et al. 2000) and in the disk of the Galaxy (Bowen et al. 2008).

FIMS/SPEAR aboard South Korea’s STSAT-1 satellite undertook all sky spectral-imaging in the wavelength range 900–1150 Å and 1350–1750 Å (Seon et al. 2011; Jo et al. 2017, 2019). The authors fit high latitude data to a collisional-ionization equilibrium (CIE) model and find a plasma temperature of 2×10^5 K and a vertical emission measure of $\int n_e(z)^2 dz \approx 0.01 \text{ cm}^{-6} \text{ pc}$. For these parameters, the free-free emission amounts to < 1 CU in the FUV band. The most prominent line in the spec-

trum towards the Galactic poles is the CIV doublet with a strength of 4,600 LU. Separately, Martin et al. (1991) report a similar detection towards the Lockman hole – a region with a very low (lowest?) H I column density. We will thus assume that 4,600 LU is not reflected light but is genuine emission from high-latitude HIM.

In order to determine the total emission from the HIM we need to account for fainter lines and continuum (free-bound, primarily). To this end, we used CHIANTI (Dere et al. 1997; Del Zanna et al. 2021) and obtained the CIE spectrum of a solar-abundance plasma at $T = [1, 2] \times 10^5$ K. We integrated this model with the effective area of the GALEX FUV detector (see Figure 1) and found that the CIV emission is [40%, 80%] of the emission integrated over the FUV band. Taking the average we find the line emission from the HIM contributes $1.875 \times 4600 = 8625$ LU to the FUV band. The effective width of the GALEX FUV band is 255 Å (Table 3). Thus, the HIM contribution to the FUV background is 34 CU.

4.3. Low-velocity Shocks

Shocks are a central topic in the study of the ISM. The post-shocked gas cools via line emission, free-bound and free-free emission. Spectral libraries of cooling gas have been published with increasing sophistication; see Raymond (1979), Shull & McKee (1979) and Sutherland & Dopita (1993). Shocks with low-velocities, $v_s \lesssim 100 \text{ km s}^{-1}$, cool via lines of H I (in decreasing order, Ly α , two-photon continuum, H α). In fact, one of the earliest and unambiguous detection of two-photon emission was from a Herbig-Haro object with a 100 km s^{-1} shock (Brugel et al. 1982; see also Dopita et al. 1982).

With some interest I note that two-photon emission was invoked in a recent investigation of the fascinating 30°-long H α arc in Ursa Major (McCullough & Benjamin 2001; Bracco et al. 2020). Separately, Fesen et al. (2021), using GALEX FUV observations along with H α and radio imaging, uncovered three very large supernova remnants. In both cases, the underlying cause of two-photon emission is low-velocity shocks, $v \lesssim 100 \text{ km s}^{-1}$.

All high velocity shocks eventually cascade to low-velocity shocks. In fact, the classical explanation for the observed $\approx 10 \text{ km s}^{-1}$ velocity dispersion of the CNM is the stirring of the ISM by supernovae (§12.2c, Spitzer 1978; Kim & Ostriker 2015). The mass of the Galactic H I gas is $M_{\text{HI}} = 3 \times 10^9 M_\odot$ (Chapter 1 of Draine 2011). The Galactic supernova (SN) rate is estimated to be one per century or $\dot{E}_{\text{SN}} = 3 \times 10^{41} \text{ erg s}^{-1}$, assuming $E_0 = 10^{51} \text{ erg}$ per SN. Let η be the conversion efficiency of SN energy that goes into the stirring of the atomic phases and let σ_{HI} be the effective rms velocity of

CNM+WNM. Then the mean time between successive stirrings is

$$\tau_{\text{HI}} = \frac{1/2 M_{\text{HI}} \sigma_{\text{HI}}^2}{\eta \dot{E}_{\text{SN}}} \approx 10^{13} \eta^{-1} \sigma_6^2 \text{ s},$$

where $\sigma_{\text{HI}} = 1 \times 10^6 \sigma_6 \text{ cm s}^{-1}$. Locally, the vertical column density towards the Galactic poles is $N_H \approx 2 \times 10^{20} \text{ atom cm}^{-2}$ (Lockman & Gehman 1991). Thus, the rate of successive SN impacts in a vertical column is

$$\mathcal{F}_{\text{SN}} = N_H / \tau_{\text{HI}} = 2 \times 10^7 \eta \sigma_6^{-2} \text{ atom cm}^{-2} \text{ s}^{-1}. \quad (1)$$

In order to convert \mathcal{F}_{SN} to two-photon decays we make the following (conservative) assumptions: (1) we restrict to shocks with initial velocity, $v \gtrsim 100 \text{ km s}^{-1}$. Such shocks will pre-ionize the ambient gas (Raymond 1979; Shull & McKee 1979). (2) In the post-shocked region each H ion undergoes only one recombination, (2) about a third of the recombinations lead to two-photon emissions and (3) following recombination, no H atom is collisionally excited to the 2s state or 3p state. With these assumptions, the columnar rate of two-photon decay is $\mathcal{R} \approx 1/3 \mathcal{F}_{\text{SN}}$.

McKee & Ostriker (1977), in the framework of the 3-phase model for the ISM, found $\eta = 0.05$. Kim & Ostriker (2015) carry out a detailed simulation and find that each SN (with $E_0 = 10^{51} \text{ erg}$) has, at the onset of the formation of radiative shells (“snowplow” phase), a velocity, $v_{\text{sf}} = 200 \text{ km s}^{-1}$ and a momentum of $p_{\text{sf}} = 2 \times 10^5 n_0^{-0.15} M_{\odot} \text{ km s}^{-1}$ where n_0 is the particle density of the medium into which the SN exploded. If we assume that all this momentum results in stirring of clouds then $\eta = 1/2(p_{\text{sf}}/\sigma_{\text{HI}})\sigma_{\text{HI}}^2/E_0 \approx 2\sigma_6\%$. We adopt mean of the two estimates $\eta = 0.035$ and find $\mathcal{R} = 0.23 \times 10^6 \sigma_6^{-2} \text{ decay cm}^{-2} \text{ s}^{-1}$. This corresponds to an FUV brightness of 20 CU.

5. FLUORESCENCE OF $\text{Ly}\beta$ PHOTONS

In the Solar system, two-photon emission is a result of fluorescence of solar $\text{Ly}\beta$ absorbed by H atoms. There is a rich literature of both theory and observations related to diffuse $\text{Ly}\alpha$ in the Solar system and less so on $\text{Ly}\beta$. Following excitation by a $\text{Ly}\beta$ photon to one of the 3p levels the atom can relax to the ground state by emitting a $\text{Ly}\beta$ photon (we denote the corresponding A-coefficient by A_{31}) or de-excite to the $2s^2S_{1/2}$ state by emitting an $\text{H}\alpha$ photon (A_{32}); see Figure 3. The branching ratio to emit $\text{Ly}\beta$ is $B = A_{31}/(A_{31} + A_{32}) = 0.88$. We let $\eta_{\text{H}\alpha} \equiv A_{32}/A_{31} \approx 1/7.4$. For higher order Lyman series photons the probability to reach the $2s^2S_{1/2}$ level is smaller. Furthermore, an inspection of the solar spectrum shows that the intensity of the higher lines is

smaller than that of the $\text{Ly}\beta$ line. As a result, we simplify by restricting our analysis to only $\text{Ly}\beta$ excitations.

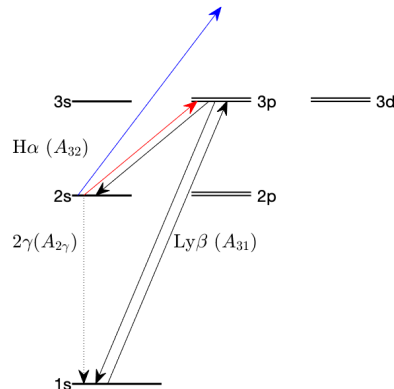


Figure 3. Partial Grotrian diagram for H I (not to scale). An H atom excited by $\text{Ly}\beta$ to 3p can de-excite to ground state by emitting $\text{Ly}\beta$ (probability of $\approx 7/8$) or de-excite to the $2s^2S_{1/2}$ level by emitting $\text{H}\alpha$. An atom in the 2s state can be further excited by Balmer photons (e.g. $\text{H}\alpha$, red arrow) or bound-free process (blue arrow); see §B.2 for discussion.

The solar $\text{Ly}\beta$ line has a velocity profile with two horns separated by about 0.33 \AA and a full-width-at-zero of 1 \AA (Figure 4). In other words, the velocity width of $\text{Ly}\beta$ is quite narrow, $\pm 50 \text{ km s}^{-1}$. The geo-coronal H atoms, with respect to the Sun, have essentially zero radial velocity and a thermal velocity full-width at half-maximum (FWHM) of 7 km s^{-1} . The H atoms in the IPM have a mean velocity of -24 km s^{-1} with respect to the Sun. The thermal velocity spread of those H atoms is 18 km s^{-1} . Thus, H atoms in the geo-coronal and IPM can readily absorb solar $\text{Ly}\beta$ photons.

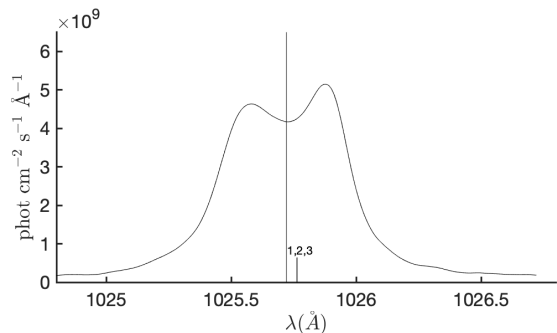


Figure 4. The profile of solar $\text{Ly}\beta$ obtained from the SOHO missoin (Lemaire et al. 2015). Notice the low continuum level (see Figure 2 of Dudok de Wit et al. 2005 for an annotated EUV/FUV solar spectrum). The vertical line marks the rest wavelength of $\text{Ly}\beta$. The three vertical ticks labeled “1,2,3” mark the wavelengths of three resonance lines of O I which have Bowen fluorescence with $\text{Ly}\beta$ (see §B.3).

A linear relation exists between the intensity at the valley center and the integrated Ly β emission. This relation allows solar astronomers to conveniently infer the zero velocity (central) Ly β intensity from integrated Ly β observations. Over the period 1996–2009 (solar cycle 23), the central photon flux density at 1 AU varied from 4×10^{10} phot cm $^{-2}$ s $^{-1}$ nm $^{-1}$ to 10×10^{10} phot cm $^{-2}$ s $^{-1}$ nm $^{-1}$ (Lemaire et al. 2015). We adopt the minimum flux for our fiducial value. We also switch to the traditional Å unit for the differential wavelength and thus $F_\lambda(\beta, v = 0) = 4 \times 10^9$ phot cm $^{-2}$ s $^{-1}$ Å; here, v is the radial velocity between the absorbing H atoms and the mean velocity of the Sun. The spectral frequency flux density is

$$F_\nu(\beta, v = 0) = 1.4 \times 10^{-3} \text{ phot cm}^{-2} \text{ s}^{-1} \text{ Hz}^{-1}. \quad (2)$$

Going forward, we use the short hand $F_\nu(\beta, v = 0) = F_\nu(0)$ and so on.

The frequency-dependent absorption cross-section is $\sigma_{lu}(\nu) = (\pi e^2)/(m_e c) f_{lu} \phi_\nu$ where l (u) stands for lower (upper) levels, f_{lu} is the oscillator strength and ϕ_ν is the probability distribution as a function of frequency for the absorption process, $\int \phi_\nu d\nu = 1$. The Ly β column densities in the IPM and exosphere are modest and so we can entirely ignore the “damping” or Lorentzian wings. If, as it happens to be the case, the solar Ly β photon intensity is constant over the thermal frequency spread of Ly β absorption frequency of terrestrial H atoms then $F_\nu = F_\nu(0)$ and the rate of excitation per atom is

$$\mathcal{R} = \int F_\nu \sigma_{lu}(\nu) d\nu = F_\nu(0) \frac{\pi e^2}{m_e c} f_{lu} \text{ atom}^{-1} \text{ s}^{-1}. \quad (3)$$

Consider a medium that is optically thin and has sufficiently low particle density so that the probability of an H atom colliding with another particle, particularly a proton, over a duration of $A_{2\gamma}^{-1}$, is negligible. Using Equations 2 and Equation 3 and noting that the oscillator strength is $f_{lu} = 0.079$ we find the total rate of excitation to the 3p state is

$$R_\beta = 2.94 \times 10^{-6} d_{\text{AU}}^{-2} \text{ atom}^{-1} \text{ s}^{-1}. \quad (4)$$

The corresponding Ly β photon surface brightness is $L_\beta = \mathcal{R}_\beta N_H$ where N_H is the hydrogen column density, along the line of sight.

The ratio of the solar Ly α to Ly β intensity (with intensity expressed in energy units and not photons) ranges from 50 (solar maximum) to 80 (solar minimum); see (Lemaire et al. 2012). Thus the photon flux ratio of Ly β to that of Ly α , hereafter η_\odot , ranges from 1/95 to 1/60. We adopt, the harmonic mean $\eta_\odot = 1/73$. The ratio of $\lambda^2 f_{lu}$ for the two lines is 7.4. Thus, for optically

thin medium, $L_\beta \approx L_\alpha/540$. The surface brightness in H α , $L_{H\alpha} = \eta_{H\alpha} L_\beta \approx L_\alpha/4000$. If, the medium has low-density (see §7.2), which is the case for IPM and exosphere, then every H α emission is accompanied by two-photon emission. Thus, $L_{2\gamma} = L_{H\alpha}$, where both quantities are expressed in photon units.

However, in the inner solar system, there is a copious flux of solar Balmer photons (H α , H β ...). As can be seen from Figure 3 an H atom in the 2s level can be further excited to higher levels by absorbing a Balmer photon (“solar pumping”). In §B.2 we show that this process results in a pumping rate, $A_p \approx 2.2 d_{\text{AU}}^{-2} \text{ s}^{-1}$ where d_{AU} is the distance of the hydrogen atom from the Sun in units of AU. An H-atom, upon absorption of Ly β , now has several outcomes: decay to ground state by emitting Ly β , decay to 2s followed by pumping back to 3p and then followed by decay to ground state by emitting Ly β or photo-ionized or excited to 4p state or finally decaying to ground-state via two-photon continuum. So, instead of having a single branching ratio we now have several. The bottom line is that solar pumping reduces the two-photon emission probability by $p_{2\gamma} = A_{2\gamma}/(A_{2\gamma} + A_p)$. Incidentally, this means in the inner solar system Ly β fluorescence will have reduced two-photon emission but brighter H α emission (cf. Shih et al. 1984).

6. INTERPLANETARY MEDIUM

The entire Solar system is moving into a local interstellar cloud at a velocity of about 25 km s $^{-1}$. From high-resolution spectroscopic UV studies the following properties of the interstellar cloud have been deduced: neutral H density of 0.1 cm $^{-3}$, temperature of 7000 K and 50% ionization fraction (Frisch et al. 2011; Gry & Jenkins 2017). These properties seem to have physical attributes similar to the WNM, albeit with a high fractional ionization and also a low column density. While astronomers refer to this cloud as the “very local” ISM (VLISM) planetary astronomers call this medium as the interplanetary medium (IPM).

The Sun has a weak wind, about $10^{-14} M_\odot \text{ yr}^{-1}$. The wind is correlated with solar activity and also has dependence on solar latitude and longitude (Pröls & Bird 2004). At 1 AU, the typical properties are as follows: electron density, n_e of 3–10 cm $^{-3}$, magnetic field strength of 10–370 μG and temperature of 10^5 K. By the time the wind reaches Earth it is supersonic, $v_{\text{wind}} \approx 500 \text{ km s}^{-1}$.

The fast solar wind comes to equilibrium with the slow moving interstellar medium by undergoing a shock – the so-called solar wind termination shock (SWTS). In the parlance of planetary astronomers, the surface separating the shocked solar wind and the interstellar gas is

called the heliopause (aka “contact discontinuity” for astronomers). Thanks to the Voyager missions we know that the SWTS is located at 90 AU while the heliopause is at 120 AU.

The neutral particles of the VLISM/IPM are not affected by the shock fronts and drift into solar system. The incoming H atoms scatter solar Ly α and thereby creating a Ly α haze over the sky, first detected by OGO-5 (see Bertaux & Blamont 1971; Thomas & Krassa 1971). The direction of the wind has been precisely determined (e.g., Frisch et al. 2013; Gry & Jenkins 2017). The “downwind” direction in ecliptic longitude (λ) and latitude (β) coordinates is 79° and -5° which corresponds to Galactic coordinates $l = 185^\circ$ and $b = -12^\circ$. The upwind direction, $l = 5^\circ$ and $b = 12^\circ$, corresponds to a direction just “above” Scorpius constellation but “below” Ophiuchus. The H atoms are photo-ionized ($\mathcal{R}_{\text{pi}} = 0.8\text{--}0.17 \times 10^{-7} d_{\text{AU}}^{-2} \text{s}^{-1}$) or undergo charge exchange⁵ ($\mathcal{R}_{\text{ce}} \approx 4 \times 10^{-7} d_{\text{AU}}^{-2} \text{s}^{-1}$) as they approach the sun. The Solar Wind ANistropies (SWAN) instrument aboard the SOLar Heliospheric Observatory (SOHO) uses a hydrogen cell to map the Ly α haze (see §G for summary). The SWAN sky image⁶ is highly asymmetric, bright in the upwind direction and faint in the downwind direction.

6.1. Measurements

Voyager-2 was launched on 1977 August 20. One month later (heliocentric distance⁷ of 1.02 AU) the UV spectrometer was pointed to $\alpha = 324^\circ$ and $\delta = -23^\circ$ and detected Ly α at $722 \pm 0.5 R$, Ly β at $2 \pm 0.16 R$ and Helium 584 Å at $3.8 \pm 0.04 R$ (Sandel et al. 1978). Long observations of several high Galactic latitude fields were undertaken in February and March, 1981 (8.4 AU). These observations detected not only Ly β but also higher order Lyman lines (Holberg 1986). Of interest to us were $L_\alpha = 1080 R$ and $L_\beta = 2.4 R$. The ratio between Ly α and Ly β seems to be consistent with that expected for optically thin medium (§5). The New Horizons mission also carried a UV spectrometer and detected Ly α surface brightness of $550 R$ at a heliocentric distance of 7.6 AU decreasing to $100 R$ at 38 AU (Gladstone et al. 2018) – confirming that peak Ly α production takes place in 2–5 AU (in the upwind direction). Incidentally, the latest report from New Horizons (now at 48 AU) is the

detection of an isotropic Ly α glow with a brightness of about $43 R$ and ascribed to Ly α leaking from the vicinity of distant hot stars (Gladstone et al. 2021).

We now summarize this section. From our vantage point, in the “upwind” direction of the IPM, we see $L_\beta = 2.4 R$. The expected two-photon decay rate is $\eta_{H\alpha} L_\beta = 0.33 R$. The corresponding brightness in the FUV band is about 28 CU.

7. THE ATMOSPHERE OF EARTH

The same solar Lyman photons that excite the IPM also excite hydrogen atoms in the thermosphere and the exosphere. The key regions of the atmosphere relevant to this section are thermosphere, exosphere and ionosphere (see §C, §D and §E for background summaries). In the thermosphere (100–600 km) atomic hydrogen is a minority species. Solar EUV heat up this region by cleaving molecules. At the top of the thermosphere (“exobase”) the temperature is high enough for H and He atoms to achieve sufficiently high thermal velocity to escape from Earth. The resulting slowly outflowing exosphere is detectable to distance beyond the lunar orbit.

Ly β , due to a coincidence, can also excite atomic oxygen (aka Bowen fluorescence; see §B.3). Next, as will be explained below, two-photon production (but not H α) is suppressed at proton densities higher than 10^4 cm^{-3} . As a result of these two complications, our estimate of two-photon brightness from the thermosphere and the exobase is uncertain. We can, however, with confidence, estimate the two-photon output from a height of 1500 km and above. It is this estimate that is presented in Table 2 under the heading “exosphere”.

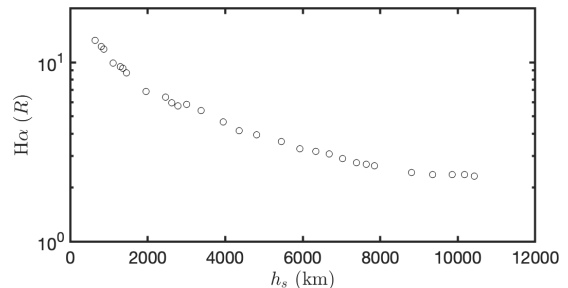


Figure 5. Representative zenith angle scan of geocoronal H α undertaken with WHAM at Kitt Peak National Observatory at dusk shown as a function of shadow height, h_s . The WHAM data are from Nossal et al. (2008) and obtained during February 2000 (solar maximum).

7.1. Ground-based observations of geocoronal H α

WHAM, during dusk and dawn, undertook scans of the sky in H α as a function of zenith angle for aeronautical studies. These scans, by tradition, are displayed as a

⁵ Following charge exchange the H atom acquires the erstwhile large velocity of solar wind protons and can thus no longer absorb solar Ly β flux with its narrow velocity width.

⁶ <http://swan.projet.latmos.ipsl.fr/>

⁷ The distance to Voyager-2 was computed using a tool provided at <https://omniweb.gsfc.nasa.gov/coho/helios/heli.html>

function of “shadow height” (Figure 6). Next, note that within the shadow cylinder, in the absence of multiple scattering, no $H\alpha$ emission will take place. However, $Ly\beta+OI$ and $Ly\alpha$ is clearly seen by LEO missions looking “upward” (see §7.3 and §B.3). Detailed modeling (Bishop et al. 2001) show, in fact that, within the thermosphere (100-500 km) scattered $Ly\beta$ is comparable to the incident flux. Note also that “cascade” or contribution to $H\alpha$ due to recombinations from higher levels is estimated to be less than 10% (Bishop et al. 2001). So, it is reasonable to assume that $H\alpha$ is essentially due to fluorescence of $Ly\beta$.

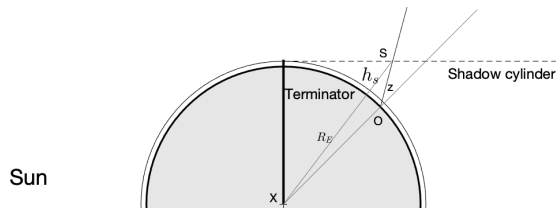


Figure 6. Illustration to explain the concept of shadow height or shadow altitude. The thick black circle represents the surface of Earth (radius, R_E) while the lighter circle represents the height at which $Ly\beta$ is absorbed (about 100 km; primarily by molecular oxygen). The Sun (left) casts a cylindrical shadow (dashed lines) to the right. The line-of-sight of the observer (“O”) bearing zenith angle z intersects the shadow cylinder at “S”. The “shadow” height, h_s , is the radial distance above the Earth’s surface to point S, $h_s = x_s - R_E$ where x_s is the length of segment XS.

The $H\alpha$ brightness at large shadow heights (cf. Figure 5) was found to be $1.5 R$ at solar minimum and twice that at solar maximum (Nossal et al. 2008, 2019). The corresponding two-photon brightness, using the formulation discussed in §3, is 85 CU which, when summed with other sources of two-photon emission (§4, §6), would exceed the level of the offset emission of 120–180 CU. This apparent contradiction is a result of ignoring a key physical process that arises in dense regions and is discussed next.

7.2. Collisional Mixing of $2s$ and $2p$ states

Given the milli-eV energy difference, a collision can easily shift an H atom from the $2s$ to one of the two $2p$ states after which the atom will, in short order ($A_{21}^{-1} \approx 2$ ns), emit a $Ly\alpha$ photon and thereby suppress two-photon emission. For neutral particle colliders we adopt a “hard sphere” model and set the cross-section to $\sigma = 10^{-16}$ cm². We find that the time scale for collisions is longer than $A_{2\gamma}^{-1}$ throughout the thermosphere (see right panel of Figure 14). It turns out that the slower moving protons are more effective than electrons in effecting these (primarily) angular-momentum chang-

ing $2s \rightarrow 2p$ transitions (Purcell 1952; see §B.1). A reasonable night-time temperature for the thermosphere is $\approx 1,000$ K (§E). Let q_{e+p} be the sum of the collisional coefficients for electrons and protons.⁸ Matching the inverse mean time between collisions $n_p q_{e,p}$ to $A_{2\gamma}$ yields the critical density $n_{crit} = A_{2\gamma}/q_{e,p} \approx 10^4$ cm⁻³ where n_p is the mean proton density. The production of two-photon becomes inefficient by $(1 + n_p/n_{crit})$. From Figure 15 we conclude that two-photon emission is suppressed below 1,200 km. However, note that this collisional mixing does not affect the production of $H\alpha$ photons.

7.3. Observations of $Ly\beta$ in the Thermosphere

Two missions, both in low-earth (height of about 600 km) orbit, Space Test Program 78-1 (STP 78-1; aka “Solwind”) and EURD aboard the Spanish Minisat-01 mission (Morales et al. 1998), measured $Ly\beta$ brightness. Details of the missions are summarized in §F.

At the beginning of this section we alerted the reader of Bowen fluorescence of $Ly\beta$ by O I. In detail, three lines of O I (hereafter, the “trio”) lie only about $+8$ km s⁻¹ of the rest wavelength of $Ly\beta$ (see Figure 13) and are thus readily excited by solar $Ly\beta$ photons (see Figure 4). Each such excitation results in re-emission of the incident photon (71%) which will be indistinguishable from $Ly\beta$ or fluorescence via emission of the O I 1304 Å triplet (see Figure 13). Next, the sum of the oscillator strengths for the trio is $f_{trio} = 0.0201$ which can be compared with $f_\beta = 0.0791$, the oscillator strength for $Ly\beta$. However, as can be seen from Figure 14, O I dominates over H I up until 800 km.

The measurements are summarized in Table 1. The observed upward $Ly\beta+OI$ brightness sets an upper limit to the surface brightness of $Ly\beta$. The brightness of the resonant $\lambda 1304$ Å (note that terrestrial O I atoms also scatter solar 1304 Å photons) means that a good fraction of the observed $Ly\beta+OI$ must be due to O I. On the other hand, for optically thin conditions, the ratio of $Ly\alpha$ to $Ly\beta$ is 400 which should be compared with 540 (§5). If we assume optically thin conditions for $Ly\beta$ then we would expect 3/4 of the upward brightness is due to $Ly\beta$.

The downward $Ly\beta+OI$ surface brightness of $2.3 R$ and the (upward) ground-based geo-coronal $H\alpha$ emission of $1.5 R$ (solar minimum) or $3 R$ (solar maximum) can only be reconciled by ascribing most of the ground-based (integrated) $H\alpha$ emission to an altitude above the

⁸ Ions such as O^+ are even more effective because of their slower velocities. However, by 1,000 km height the dominant species is H and not O; see Figure 14.

Table 1. STP 78-1 & EURD observations of night glow

line	“Up” (R)	“Down” (R)
Ly β +OI	8.76 ± 0.3	2.3 ± 0.23
Ly α	3533 ± 5.8	1712 ± 4.7
O I 1304	7.1 ± 0.4	53.8 ± 1.3
O I 1356	< 2	52.2 ± 0.8

NOTE— Restricting to absolute zenith angle of $< 70^\circ$, EURD detected, at night time, Ly β at a level of $6.4 R$ (López-Moreno et al. 2001).

orbital height of Solwind. However, Bishop et al. (2001) argue that bulk of this H α arises from atomic hydrogen between 100 and 500 km. Their model hydrogen column density over this range of height of $6 \times 10^{13} \text{ cm}^{-2}$ is five times larger than that provided by the standard MSIS (Mass Spectrometer and Incoherent Scatter radar) model (see Figure 14). Overall, the situation is unsatisfactory. There is a compelling need for space-based measurements in H α (§10).

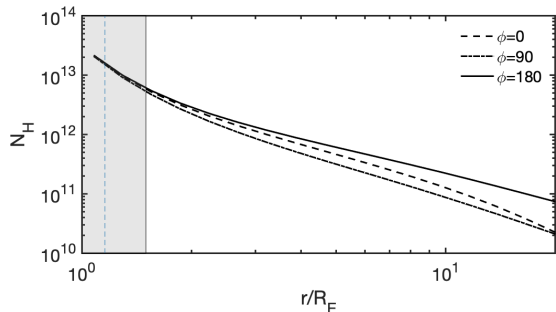


Figure 7. Top: The column density profile of H atoms as derived from *SWAN-SOHO* measurements (Baliukin et al. 2019). Here, r is the distance from center of Earth and R_E is the radius of Earth. The dashed vertical line marks height of 1,000 km. Owing to the angular resolution of *SWAN* the model is not reliable for radius less than $1.5 R_E$ (shaded region). ϕ is the angle between line-of-sight and the direction to the Sun. Thus the night-time radial profile is described by $\phi = 180^\circ$ model whereas $\phi = 0^\circ$ applies to the model at noon time. The exosphere has a larger radial extent on the night side, compared to the day side (“geotail”). The model data were supplied by I. Baliukin.

8. THE EXOSPHERE

We use data from two missions: the afore-mentioned *SWAN* on *SOHO* and the *IMAGE* missions, the summaries for which can be found in §G. As can be seen from Figure 7 the hydrogen column density above 1,000 km

is approximately 10^{13} cm^{-2} . The corresponding central optical depth in Lyman- β is given by

$$\tau_0 = 0.32 \left(\frac{N_l}{10^{14} \text{ cm}^{-2}} \right) \left(\frac{5 \text{ km s}^{-1}}{b} \right) \quad (5)$$

where $b = \sqrt{2}\sigma_v$ and σ_v is the Gaussian velocity width. Thus, τ_0 is less than unity and so the two-photon brightness is $\eta_{H\alpha} L_\beta$.

8.1. Ly β scattering during night time

We now compute Ly β scattering during Earth eclipse as observed by a satellite in a circular orbit of height h , at local midnight (see Figure 8 for geometry). Not much error is made in replacing the conical umbra with a cylindrical shadow. From trigonometry we find $r^2 = r_s^2 + l^2 + 2r_s l \cos(z)$ where $r_s = R_E + h$ is orbital radius of the satellite and l is the distance measured from the satellite along a given line-of-sight (see Figure 8 for geometry). We integrate the column of hydrogen along a line-of-sight bearing angle z to obtain N_H . The resulting Ly β photon surface brightness is $L_\beta = (1/4\pi)N_H \mathcal{R}_\beta$ where \mathcal{R}_β is the per atom rate of Ly β excitation (Equation 4). The corresponding two-photon emission per atom rate is $(1 - Bp_{2\gamma})\mathcal{R}_\beta$ (see §B.2).

In Figure 8 we display $L_{2\gamma}$ as a function of the satellite zenith angle. We see that in our simple single-scattering model there is no two-photon emission at zenith. However, there is evidence of Ly β photons in the shadow cylinder. First, the upward looking Ly β +OI (§7.3) is substantial, $\approx 8 R$. Next, O I $\lambda 1304 \text{ \AA}$ triplet is seen by HST at local midnight. This bright line is a result of Bowen fluorescence of O I powered by Ly β photons (§C). Clearly, Ly β must be scattered into the shadow cylinder.

We make the simplistic assumption that the scattered photons “fill up the trough” in Figure 8. *GALEX* observations were conducted for less than a quarter of the orbit. Thus the observing window is $z < 45^\circ$. The mean model brightness over this window is $0.4 R$ which corresponds to 34 CU.

9. SUMMING UP

We started the paper by noting that at high latitude some 120–180 CU of the *GALEX* FUV could not be accounted by EBL and DGL (§2). In successive sections (§4–§8) we undertook a systematic examination of two-photon emission from the WIM, low-velocity shocks, and the Solar system as well as line emission from the HIM. The resulting estimates are summarized in Table 2 above. We find that 118–139 CU of the *GALEX* FUV background can be attributed to conventional sources. Given the ramifications of this conclusion we next examine the uncertainties in the entries in Table 2.

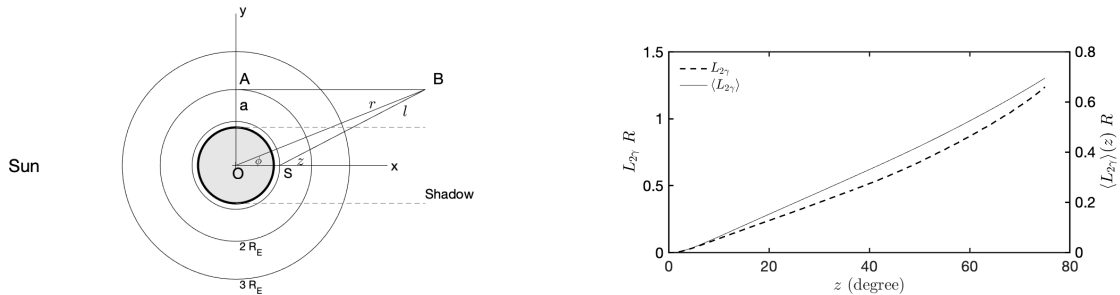


Figure 8. (*Left*): Geometry of the Exosphere. The coordinate system is defined by x away from the Sun, y towards the terrestrial North pole and Earth at the origin. The circles are successively: the surface of Earth ($r = R_E$; dark line), $r_s = R_E + h$ where h is the height of a satellite (marked “S”); radius of $2R_E$ and $3R_E$. The impact parameter, a , is the segment OA. The umbra cast by Earth is a cone with a depth of $215 R_E$. We simplify by replacing the umbra-penumbra combination with a cylinder (dashed lines; “Shadow”). Consider a line-of-sight originating from the aforementioned satellite going towards point B (which is at radius r). Let z be the zenith angle, measured from x axis in a counter-clockwise fashion, and ϕ the corresponding geo-centric polar angle. l (SB) is the distance measured from the satellite to point B. (*Right*): The model two-photon surface brightness in units of Rayleigh expected at night time as a function of the fraction of the sky, as measured along angle z of the satellite.

Table 2. Inventory of diffuse FUV emission

Source	tracer	value	\mathcal{B} (CU)
WIM	H α	$0.4 R$	23
HIM	C IV	8625 LU	34
Low-velocity shocks ^a	model	-	20
IPM ^{b,c}	Ly β	$2.4 R$	7–28
Exobase ^d	model	??	??
Exosphere ^c	model	-	34
Total			118–139
Offset component	<i>GALEX</i>	-	120–180

NOTE—The source of emission is two-photon for all entries save the HIM (for which the source is line emission). ^aThis entry is computed from a theoretical model. Restricted to shocks which are at least 100 km s^{-1} . ^bThe intensity of the IPM is brightest in the upwind direction and faintest in the opposite direction. ^cThis contribution scales directly with solar activity (EUV flux). Estimates presented here were computed for solar minimum. ^dThis refers to the region with height from 1200 km to 1500 km.

9.1. Uncertainties

In my view, the contributions from the WIM, the HIM and IPM rest on reliable measurements and robust theory (WIM: classical theory of recombination; HIM: direct observations; IPM: basic physics, optically thin situation and robust measurements of density profile of IPM H atoms)

By far the biggest uncertainty is the contribution from the exobase region. Recall that H I dominates over O I starting at 700 km (see §C) and the model for the density of H atoms deduced from SWAN or IMAGE is reliable

only above 1500 km (see §G). Below height of 1200 km the high proton density suppresses two-photon decay (§7.2). Thus, Ly β scattering of H atoms below height of 1200 km results in H α but no two-photon continuum. H atoms in the annulus between 1200 and 1500 km will fluoresce and produce both H α and two-photon continuum. For short-hand we refer to this region as the exobase. Since we lack reliable measurements for atomic hydrogen in this region there is no numerical entry for exobase in Table 2.

Another notable uncertainty is the contribution of two-photon emission from low-velocity shocks. We break this uncertainty in two parts. First, is the uncertainty in the efficiency factor of supernova shocks, η (see §4.3). We took the average of two estimates, $\eta = [0.02, 0.05]$. This directly translates to factor of 2.5 uncertainty in the corresponding entry in Table 2. Next, we remind the reader that we have not included contributions from “lesser” shocks, e.g. stellar winds and novae and spiral density shocks. In this spirit, we acknowledge ignoring contribution to photon emission from shocks due to infall of gas into the disk. While the average infall rate does not compete with supernova shocks the infall is localized – the intermediate and high velocity cloud system (Wakker & van Woerden 1997). Along these lines we note that the integrated spectrum towards the North Celestial Pole (NCP) shows a constant $N_{\text{HI}}(v)v^2$ out to velocity of 80 km s^{-1} and significant infall (Kulkarni & Fich 1985). Note that the latter feature is not seen towards the SCP, another manifestation of localized flows.

Finally, the two-photon emission from the Earth and IPM scales directly with solar EUV irradiance. This typically varies by a factor of 2.5 over a solar cycle. In computing the contribution from the exosphere we

adopted the solar minimum value for solar $\text{Ly}\beta$ irradiance (Equation 2).

We conclude that a significant fraction, say two-third, and perhaps even all of the offset component can be accounted for by conventional sources discussed in this paper. We cannot rule out that a fraction of the offset emission is from exotic sources such as decay of dark matter but Occam’s razor suggests otherwise.

9.2. Global $\text{H}\alpha$ constraint

A question raised by the referee is the constraint on two-photon emission provided by observations of diffuse $\text{H}\alpha$. Let X be the photon ratio of two-photon emission to $\text{H}\alpha$ emission. For recombination is X is $[0.63, 0.72, 0.85]$ for $T = [5, 10, 20] \times 10^3$ K. For $\text{Ly}\beta$ fluorescence in optically thin and low density medium ($n_p \ll 10^4 \text{ cm}^{-3}$), $X = 1$. In contrast, $X \rightarrow 0$ for high density medium (e.g. thermosphere). HIM contributes to the FUV emission but has neither an associated $\text{H}\alpha$ emission or two-photon continuum. In contrast, $X \rightarrow 0$ for post-shocked partially ionized “warm” ($10^4 \lesssim T \lesssim 10^5$ K) gas. In such gas, the excitation is primarily to the $n = 2$ level and so the cooling is via $\text{Ly}\alpha$ and two-photon continuum; see [Kulkarni & Shull \(2022\)](#) for further cooling curves.

Subtracting contributions from the HIM and two-photon continuum exosphere (which will have an associated $\text{H}\alpha$ but at zero topocentric velocity and readily marked as such by WHAM) we find the minimum two-photon background is 50 CU (see Table 2). Using the conversion factor computed in §3 this amounts to a two-photon surface brightness of $0.58 R$. The expected $\text{H}\alpha$ surface brightness is then $\approx 0.58 \langle X^{-1} \rangle R$ where the angular brackets stand for averaging over all emission processes.

The only facility that can approach this low surface brightness is from WHAM. The observed value at the Galactic poles is $0.5 R$ (see §4.1). However, there are two caveats that must be noted. First, some of the diffuse $\text{H}\alpha$ is reflected light. This is estimated to be 20% (see §4.1). Next, WHAM relied on velocity separation to subtract geo-coronal contribution. In effect, the WHAM methodology is well suited to measuring features which are compact in velocity space. Measuring $\text{H}\alpha$ emission that is wide in velocity would require very careful accounting of the spectral baseline. Caveats aside, reconciling the model presented here to the WHAM observations would require $\langle X^{-1} \approx 0.69 \rangle$ which, in our model, means that collisional excitations contribute more than recombinations.

10. CONCLUDING THOUGHTS

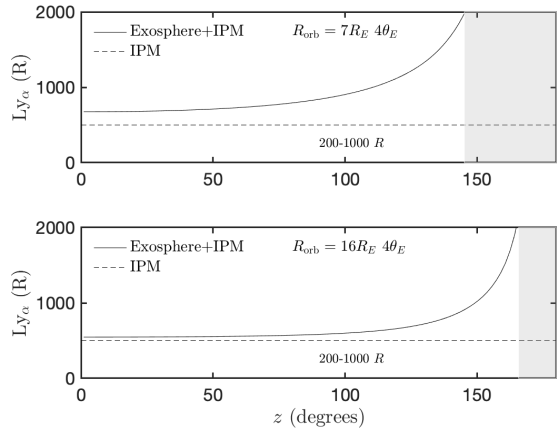


Figure 9. The expected $\text{Ly}\alpha$ background (in R) as a function of z for a satellite located in geo-synchronous orbit ($6.6 R_E$; e.g., IUE or the planned Spektr-UF mission; [Boyarshchuk et al. 2016](#)) and in High Earth Orbit (HEO; $16 R_E$). The shaded region covers the zenith angle range of 180° to $180^\circ - 4\theta_E$ where θ_E is the angular radius of Earth as seen from the vantage point of the satellite. For the purpose of this illustration the IPM $\text{Ly}\alpha$ surface brightness is fixed to $500 R$ (but see §6). Note that the two-photon continuum tracks the $\text{Ly}\alpha$ surface brightness. The two-photon continuum intensity is equal to $\text{Ly}\alpha/4000 R$. (see §5).

The diffuse FUV radiation seen at high Galactic latitudes has two components: emission that is correlated with cirrus clouds and emission that is independent of cirrus clouds. The former is attributed to stellar FUV light that is reflected by dust particles. For the latter, [Akshaya et al. \(2019\)](#) attribute 196-131 CU to emission from extra-galactic sources (galaxies, QSOs and IGM). After accounting for the extragalactic sources some 120–180 CU of emission is left – the so-called “offset” component.

This paper investigated FUV emission conventional sources: two-photon continuum from the Galactic WIM and low-velocity shocks, FUV line emission from HIM and two-photon emission our own interplanetary medium, and exosphere and the thermosphere. From Table 2 it appears that these contributions collectively can readily account for two thirds of the offset component. We did not compute emission from a number of minor processes. It is possible that the offset component can be entirely explained without resorting to speculation (e.g. decay of dark matter).

We conclude this article with a few thoughts. Apart from $\text{Ly}\alpha$ the irreducible background for FUV missions is, in our model, due to two-photon emission. Both backgrounds can be considerably reduced by placing FUV missions into a high-earth orbit (Figure 9) and by undertaking observations at satellite zenith angle, $z \lesssim 90^\circ$

and preferentially studying regions of sky centered on the down-wind direction.

The discovery of three large SNRs (Fesen et al. 2021) was made possible, in part, by the distinctive FUV signature of low-velocity shocks. Two-photon continuum is more sensitive than $H\alpha$ searches because (1) the FUV sky is dark and so diffuse emission is readily detected and (2) $H\alpha$ from low-velocity shocks is broad in velocity and also has to compete with other sources (e.g., geo-corona, IPM and WIM). Motivated thus we advocate for an FUV mission which will undertake an all-sky survey with arcsecond resolution. The resulting FUV continuum image of the sky will provide a new diagnostic for study of diffuse Galactic structures and low-velocity shocks. A concomitant effort should be modeling the collective cooling from the innumerable low-velocity shocks in our Galaxy.

For satellites in LEO, the primary airglow in FUV is due to $Ly\alpha$ and lines of oxygen. The *GALEX* FUV bandpass was designed to avoid the two strongest lines, $Ly\alpha$ and the fluorescent O I triplet (see §B.3). A small amount of the semi-forbidden 1356 Å oxygen doublet is present within the bandpass. The airglow is the smallest when the satellite is in the shadow of Earth and is pointing anti-sun. This airglow is seen by FUV instruments⁹ on HST even when pointing anti-sun, whilst in deep Earth shadow. An FUV mission in HEO would not suffer from airglow and so the background emission will be very stable. A happy by-product of such a mission would be an accurate measurement of the strength of the offset component.

Next, from the discussion in §7 it is clear that there is a tension between the amount of hydrogen in the thermosphere as deduced by modeling ground-based $H\alpha$ data and the MSIS model. Furthermore, the modeling of LEO-based measurements of $Ly\beta+OI$, complicated by Bowen fluorescence of O I, is not satisfactory. A cube-sat with an $H\alpha$ photometer offers a clean way to model the vertical distribution of hydrogen.

As can be seen from Figure 10¹⁰ the solar EUV irradiance varies on timescales of not just solar cycles but hours! This variability offers us an opportunity to probe the exosphere and the IPM. Parenthetically, we note that evidence for variability in the *GALEX* FUV data can be readily seen in discordant “sky” values for adjacent pointings of *GALEX* FUV mosaic images (e.g.,

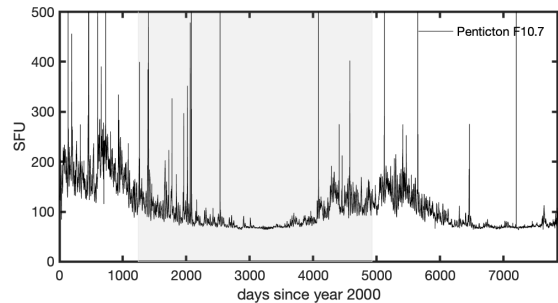


Figure 10. The solar 10.7-cm flux density (F10.7) since year 2000. The F10.7 index is widely used as a ground-based surrogate for the EUV irradiance of the Sun (see Tapping 2013). The solar minimum occurred in 2010 (say, day 3600). The shaded region is the period during which *GALEX* was operational. The vertical axis has been clipped. The short spikes can reach 2000 SFU and are probably due to magnetic reconnection. The unit SFU stands for solar flux unit and is equal to 10^4 Jy.

see Figure 2 of Fesen et al. 2021). Future FUV missions would be well advised to model the FUV background by folding in solar EUV monitoring data.

Finally the ISM-Solar system interaction is a major area of research in space sciences. For a modest funding, a ground-based facility with sensitivity ten times better than that of WHAM can be built. Solar EUV irradiance changes on a variety of timescales. With this facility, it may be possible to measure the resulting $H\alpha$ variations and thereby “plumb” the three-dimensional distribution of the IPM.

ACKNOWLEDGMENTS

I gratefully acknowledge receiving help from Ronald Reynolds; Michael Shull, University of Colorado at Boulder; E. Sterl Phinney, California Institute of Technology (Caltech); Jayant Murthy, Indian Institute of Astrophysics; Edwin J. Mierkiewicz & Matthew D. Zettergren, Embry-Riddle Aeronautical University; I. I. Baliukin, Space Research Institute (IKI), Moscow; and E. C. Stone, Project Scientist for Voyager Mission; Nikolaus Zen Prusinski, Caltech. For feedback: Ilaria Caiazzo, Caltech; Bruce Draine, Princeton University; Jerry Edelman & Christopher McKee, University of California at Berkeley; Marc Postman, Space Telescope Science Institute; and Kevian Stassun, Vanderbilt University. Finally, I am most grateful to Robert Benjamin, University of Wisconsin at Madison; Hannah Earnshaw, Caltech; Eran Ofek, Weizmann, Institute of Science; and Michael Shull for careful reading and constructive feedback. Finally, I thank the referee (anonymous) for feedback which resulted in a clearer and shorter paper.

⁹ see Figure 7.1 of the COS instrument handbook. <https://hst-docs.stsci.edu/cosihb>

¹⁰ The measurements were obtained at the Dominion Radio Astrophysical Observatory, Penticton, British Columbia, Canada and the data were obtained from <https://lasp.colorado.edu/lisird/>.

REFERENCES

- Ake, T. B. 2012, in American Astronomical Society Meeting Abstracts, Vol. 219, American Astronomical Society Meeting Abstracts #219, 241.18
- Akshaya, M. S., Murthy, J., Ravichandran, S., Henry, R. C., & Overduin, J. 2018, *ApJ*, 858, 101
- . 2019, *MNRAS*, 489, 1120
- Baliukin, I. I., Bertaux, J. L., Quémerais, E., Izmodenov, V. V., & Schmidt, W. 2019, *Journal of Geophysical Research (Space Physics)*, 124, 861
- Barnes, K. L., van Zee, L., & Skillman, E. D. 2011, *ApJ*, 743, 137
- Bertaux, J. L., & Blamont, J. E. 1971, *A&A*, 11, 200
- Bertaux, J. L., Kyrölä, E., Quémerais, E., et al. 1995, *SoPh*, 162, 403
- Bishop, J., Harlander, J., Nossal, S., & Roesler, F. L. 2001, *Journal of Atmospheric and Solar-Terrestrial Physics*, 63, 341
- Bowen, D. V., Jenkins, E. B., Tripp, T. M., et al. 2008, *ApJS*, 176, 59
- Boyarchuk, A. A., Shustov, B. M., Savanov, I. S., et al. 2016, *Astronomy Reports*, 60, 1
- Bracco, A., Benjamin, R. A., Alves, M. I. R., et al. 2020, *A&A*, 636, L8
- Brugel, E. W., Shull, J. M., & Seab, C. G. 1982, *ApJL*, 262, L35
- Chakrabarti, S., Kimble, R., & Bowyer, S. 1984, *J. Geophys. Res.*, 89, 5660
- Chance, K., & Kurucz, R. L. 2010, *JQSRT*, 111, 1289
- Deharveng, J. M., Joubert, M., & Barge, P. 1982, *A&A*, 109, 179
- Del Zanna, G., Dere, K. P., Young, P. R., & Landi, E. 2021, *ApJ*, 909, 38
- Dennison, B., Turner, B. E., & Minter, A. H. 2005, *ApJ*, 633, 309
- Dere, K. P., Landi, E., Mason, H. E., Monsignori Fossi, B. C., & Young, P. R. 1997, *A&AS*, 125, 149
- Dong, R., & Draine, B. T. 2011, *ApJ*, 727, 35
- Dopita, M. A., Binette, L., & Schwartz, R. D. 1982, *ApJ*, 261, 183
- Dove, J. B., & Shull, J. M. 1994, *ApJ*, 430, 222
- Draine, B. T. 2011, *Physics of the Interstellar and Intergalactic Medium* (Princeton University Press)
- Draine, B. T., & Bertoldi, F. 1996, *ApJ*, 468, 269
- Drake, G. W., Victor, G. A., & Dalgarno, A. 1969, *Physical Review*, 180, 25
- Dudok de Wit, T., Lilensten, J., Abouadarham, J., Amblard, P. O., & Kretzschmar, M. 2005, *Annales Geophysicae*, 23, 3055
- Duley, W. W., & Williams, D. A. 1980, *ApJL*, 242, L179
- Edelstein, J., Korpela, E. J., Adolfo, J., et al. 2006, *ApJL*, 644, L159
- Fesen, R. A., Drechsler, M., Weil, K. E., et al. 2021, arXiv e-prints, arXiv:2102.12599
- Frisch, P. C., Redfield, S., & Slavin, J. D. 2011, *ARA&A*, 49, 237
- Frisch, P. C., Bzowski, M., Livadiotis, G., et al. 2013, *Science*, 341, 1080
- Gladstone, G. R., Pryor, W. R., Stern, S. A., et al. 2018, *Geophys. Res. Lett.*, 45, 8022
- Gladstone, G. R., Pryor, W. R., Hall, D. T., et al. 2021, *AJ*, 162, 241
- Gry, C., & Jenkins, E. B. 2017, *A&A*, 598, A31
- Haffner, L. M., Reynolds, R. J., Tufte, S. L., et al. 2003, *ApJS*, 149, 405
- Haffner, L. M., Dettmar, R. J., Beckman, J. E., et al. 2009, *Reviews of Modern Physics*, 81, 969
- Haffner, L. M., Reynolds, R. J., Madsen, G. J., et al. 2010, in *Astronomical Society of the Pacific Conference Series*, Vol. 438, *The Dynamic Interstellar Medium: A Celebration of the Canadian Galactic Plane Survey*, ed. R. Kothes, T. L. Landecker, & A. G. Willis, 388
- Hamden, E. T., Schiminovich, D., & Seibert, M. 2013, *ApJ*, 779, 180
- Henry, R. C. 1991, *ARA&A*, 29, 89
- Henry, R. C., Murthy, J., Overduin, J., & Tyler, J. 2015, *ApJ*, 798, 14
- Holberg, J. B. 1986, *ApJ*, 311, 969
- Jo, Y.-S., Seon, K.-I., Min, K.-W., Edelstein, J., & Han, W. 2017, *ApJS*, 231, 21
- Jo, Y.-S., Seon, K.-i., Min, K.-W., et al. 2019, *ApJS*, 243, 9
- Jura, M. 1974, *ApJ*, 191, 375
- Kim, C.-G., & Ostriker, E. C. 2015, *ApJ*, 802, 99
- Kollmeier, J. A., Weinberg, D. H., Oppenheimer, B. D., et al. 2014, *ApJL*, 789, L32
- Kulkarni, S. R., & Fich, M. 1985, *ApJ*, 289, 792
- Kulkarni, S. R., & Shull, M. J. 2022, manuscript in prep
- Kurt, V. G., & Sunyaev, R. A. 1970, in *Ultraviolet Stellar Spectra and Related Ground-Based Observations*, ed. R. Muller, L. Houziaux, & H. E. Butler, Vol. 36, 341
- Lemaire, P., Vial, J. C., Curdt, W., Schühle, U., & Wilhelm, K. 2015, *A&A*, 581, A26
- Lemaire, P., Vial, J. C., Curdt, W., Schühle, U., & Woods, T. N. 2012, *A&A*, 542, L25
- Lockman, F. J., & Gehman, C. S. 1991, *ApJ*, 382, 182
- López-Moreno, J. J., Morales, C., Gómez, J. F., et al. 2001, *Ap&SS*, 276, 211
- Manchester, R. N., & Taylor, J. H. 1977, *Pulsars* (W. H. Freeman & Co)

- Martin, C., Hurwitz, M., & Bowyer, S. 1990, *ApJ*, 354, 220
— 1991, *ApJ*, 379, 549
- Martin, D. C., Fanson, J., Schiminovich, D., et al. 2005, *ApJL*, 619, L1
- McCullough, P. R., & Benjamin, R. A. 2001, *AJ*, 122, 1500
- McKee, C. F., & Ostriker, J. P. 1977, *ApJ*, 218, 148
- Meftah, M., Snow, M., Damé, L., et al. 2021, *A&A*, 645, A2
- Meier, R. R., Anderson, D. E., J., Paxton, L. J., McCoy, R. P., & Chakrabarti, S. 1987, *J. Geophys. Res.*, 92, 8767
- Mende, S. B., Heetderks, H., Frey, H. U., et al. 2000, *SSRv*, 91, 287
- Miller, Walter Warren, I., & Cox, D. P. 1993, *ApJ*, 417, 579
- Morales, C., Gómez, J. F., Trapero, J., et al. 1998, *Ap&SS*, 263, 393
- Morrissey, P., Conrow, T., Barlow, T. A., et al. 2007, *ApJS*, 173, 682
- Murthy, J., Henry, R. C., & Sujatha, N. V. 2010, *ApJ*, 724, 1389
- Nahar, S. N. 2021, *Atoms*, 9, 73
- Nossal, S. M., Mierkiewicz, E. J., Roesler, F. L., et al. 2008, *Journal of Geophysical Research (Space Physics)*, 113, A11307
- 2019, *Journal of Geophysical Research (Space Physics)*, 124, 10,674
- Nussbaumer, H., & Schmutz, W. 1984, *A&A*, 138, 495
- O’Connell, R. W. 1987, *AJ*, 94, 876
- Osterbrock, D. E. 1974, *Astrophysics of gaseous nebulae* (W. H. Freeman and Company)
- ØStgaard, N., Mende, S. B., Frey, H. U., Gladstone, G. R., & Lauche, H. 2003, *Journal of Geophysical Research (Space Physics)*, 108, 1300
- Paresce, F., & Jakobsen, P. 1980, *Nature*, 288, 119
- Paresce, F., McKee, C. F., & Bowyer, S. 1980, *ApJ*, 240, 387
- Prölss, G. W., & Bird, M. K. 2004, *Physics of the Earth’s Space Environment: an introduction* (Springer)
- Purcell, E. M. 1952, *ApJ*, 116, 457
- Raymond, J. C. 1979, *ApJS*, 39, 1
- Reynolds, R. J. 1990, *ApJL*, 349, L17
- 1992, *ApJL*, 392, L35
- Sandel, B. R., Shemansky, D. E., & Broadfoot, A. L. 1978, *Nature*, 274, 666
- Savage, B. D., Sembach, K. R., Jenkins, E. B., et al. 2000, *ApJL*, 538, L27
- Sciama, D. W. 1990, *ApJ*, 364, 549
- Seon, K.-I., Edelstein, J., Korpela, E., et al. 2011, *ApJS*, 196, 15
- Shih, P., Scherb, F., & Roesler, F. L. 1984, *ApJ*, 279, 453
- Shull, J. M., & McKee, C. F. 1979, *ApJ*, 227, 131
- Slavin, J. D., McKee, C. F., & Hollenbach, D. J. 2000, *ApJ*, 541, 218
- Spitzer, Lyman, J., & Greenstein, J. L. 1951, *ApJ*, 114, 407
- Spitzer, L. 1978, *Physical processes in the interstellar medium* (Wiley-Interscience), doi:10.1002/9783527617722
- Stecker, F. W. 1980, *PhRvL*, 45, 1460
- Sutherland, R. S., & Dopita, M. A. 1993, *ApJS*, 88, 253
- Tapping, K. F. 2013, *Space Weather*, 11, 394
- Thomas, G. E., & Krassa, R. F. 1971, *A&A*, 11, 218
- Wakker, B. P., & van Woerden, H. 1997, *ARA&A*, 35, 217
- Witt, A. N., Gold, B., Barnes, Frank S., I., et al. 2010, *ApJ*, 724, 1551
- Woolley, R. V. D. R. 1934, *MNRAS*, 95, 101
- Zettergren, M. D., & Snively, J. B. 2015, *Journal of Geophysical Research (Space Physics)*, 120, 8002

APPENDIX

A. TWO-PHOTON CONTINUUM

The classical reference for the two-photon spectrum is [Spitzer & Greenstein \(1951\)](#) where they invoked the two-photon process to explain the continuum of planetary nebulae. The modern reference is [Drake et al. \(1969\)](#). For the A-coefficient we use the fitting formula of [Nussbaumer & Schmutz \(1984\)](#):

$$A(y) = CY[1 - (4Y)^\gamma] + \alpha CY^\beta (4Y)^\gamma \quad (\text{A1})$$

where $y = \nu/\nu_0$, $Y = y(1 - y)$, $\nu_0 = c/\lambda_0$ and $\lambda_0 = 1215.67 \text{ \AA}$ is the wavelength of Ly α . The fit values are $\alpha = 0.88$, $\beta = 1.53$, $\gamma = 0.8$ and $C = 202.0 \text{ s}^{-1}$. Since each de-excitation results in the emission of two photons, $\int_0^1 A(y) dy = 2A_{21} = 16.4 \text{ s}^{-1}$. Noting that $A(y)$ is the probability of emitting a photon in the frequency interval $dy = d\nu/\nu_0$ we find the emissivity from a single decay to be

$$j_\nu = \frac{1}{4\pi} \frac{h\nu}{\nu_0} A(y). \quad (\text{A2})$$

Traditionally, observers use the spectral intensity as a function of wavelength, $j_\lambda = j_\nu \nu/\lambda$. The corresponding photon intensity is $n(\lambda) = j_\lambda/(hc/\lambda) \propto \nu j_\nu$. While $A(y)$ peaks at $y = 1/2$ corresponding to $\nu = \nu_0/2$ the spectral intensity j_λ peaks at 1400 \AA (Figure 1).

Table 3. *GALEX* bands & response to two-photon decay

Parameter	unit	FUV	NUV
Bandpass	\AA	1350–1750	1750–2800
FoV	deg^2	1.267	1.227
\mathcal{I}	$\text{cm}^2 \text{\AA}$	9402	45008
$\Delta\lambda_{\text{eq}}$	\AA	255	730
$n(2\gamma)$	count	0.27	0.44
CR	phot s^{-1}	309	838
$\mathcal{B}_{2\gamma}$	CU	85.1	18.4

NOTE—The vital statistics of the FUV and NUV channels are summarized in the top half of the table. Here, $\mathcal{I} = \int A_{\text{eff}}(\lambda) d\lambda$ and $\Delta\lambda_{\text{eq}} \equiv \mathcal{I}/\max(A_{\text{eff}})$. $n(2\gamma)$ is the number of photons detected in each channel for a single two-photon decay. The last two lines are the response by the two *GALEX* channels to a uniform background from a column of $10^6 \text{ decays cm}^2 \text{ s}^{-1}$. CR is the counting rate across the entire detector for such a background while $\mathcal{B}_{2\gamma}$ is the inferred surface brightness.

The *GALEX* FUV band¹¹ is formally 1350–1750 \AA while the NUV band is 1750–2800 \AA (see Table 3). At one end of the probability distribution function (Equation A1), $y \rightarrow 1/2$, the two photons have equal energy in which case the

¹¹ The blue edge was chosen to avoid Ly α from Earth and the Interplanetary Medium as well as the bright airglow O I $\lambda 1304 \text{ \AA}$ triplet. These lines are bright: as seen by HST, Ly α is 2 kR ([Ake 2012](#)) while the O I line $13 R$, even in Earth’s deep shadow.

NUV band will register two photons. At the other end, $y \rightarrow 0$, one photon will get registered in the FUV band and the other will be in the optical/infra-red (OIR) band. Integrating over $A(y)$ we find that each decay results in 0.42 photons in the 1350–1750 Å band, 0.67 photons in the 1750–2800 Å band and 0.82 in the OIR band. [If the division is done by energy then the corresponding fractions are 33%, 37% and 30%].

Morrissey et al. (2007) provide a summary of the instrumental parameters¹² as a function of λ but provide a single FoV value, Ω , for each of the two channels. For each channel, the band-pass weighted quantities for an input two-photon spectrum, is computed as follows,

$$j_\lambda = \frac{1}{\Omega \mathcal{I}} \int j_\lambda A_{\text{eff}}(\lambda) d\lambda, \quad n(2\gamma) = \frac{\Delta\lambda_{\text{eq}}}{\mathcal{I}} \int \lambda \frac{j_\lambda}{hc} A_{\text{eff}}(\lambda) d\lambda \quad (\text{A3})$$

where \mathcal{I} , the area-bandwidth product and $\Delta\lambda_{\text{eq}}$, the equivalent width, are defined in Table 3. The unit for $n(2\gamma)$ (listed in Table 3) is count, resulting from our choice of 1 sr, an area of 1 cm² and an integration time of 1 s. As can be seen from Table 3, each decay results in 0.27 photon in the FUV band and 0.44 photon in the NUV band. Consider an astronomical object emitting only via the two-photon process. Integrating over the pixels of this object’s image, the ratio of FUV to NUV count rates is expected to be about 0.37. We end this section by noting Bracco et al. (2020) undertook a similar exercise but with a somewhat different approach. The two results agree to better than 10%.

B. ATOMIC PHYSICS

B.1. *Mixing of 2s-2p states by collisions*

Recall that an H atom remains, on an average, in the 2s state for a duration of A_{21}^{-1} or about 0.12 s. This is sufficiently long that over this period the atom could get perturbed. Purcell (1952) showed that distant encounters with protons are more effective than electrons (which had been studied in earlier literature) in changing the angular momenta of H atoms. The computed collisional coefficients are given in Table 4. The resulting critical density, $\approx 10^4 \text{ cm}^{-3}$, significantly reduces the signal of the corresponding fine structure radio transitions from prime targets such the Sun or even HII regions (Dennison et al. 2005).

Table 4. Collisional Coefficients for H I $2s \rightarrow 2p$

transition	collider	q_0 (cm ³ s ⁻¹)	γ
$2s \ ^2S_{1/2} \rightarrow 2p \ ^2P_{1/2}$	p^+	2.51×10^{-4}	-0.27
$2s \ ^2S_{1/2} \rightarrow 2p \ ^2P_{3/2}$	"	2.23×10^{-4}	-0.03
$2s \ ^2S_{1/2} \rightarrow 2p \ ^2P_{1/2}$	e^-	0.22×10^{-4}	-0.37
$2s \ ^2S_{1/2} \rightarrow 2p \ ^2P_{3/2}$	"	0.35×10^{-4}	-0.37

NOTE—Collisional coefficient at temperature $T = 10^4 T_4 \text{ k}$ is given by $q = q_0 T_4^\gamma$. Condensed from Osterbrock (1974).

B.2. *Excitation of 2s level by solar photons*

Bishop et al. (2001) briefly mention the excitation of H atoms in 2s state by solar Balmer photons. Here, in addition, we consider bound-free ionization.

Excitation by H α and H β (bound-bound). An H atom in the $2s \ ^2S_{1/2}$ state (level degeneracy, $g_l = 2$) can be excited by bound-bound process, for instance by absorption of a solar H α photon. The excitation is then either to $3p \ ^2P_{1/2}$ ($g_u = 2$) or $3p \ ^2P_{3/2}$ level ($g_u = 4$). The oscillator strength, $f_{lu} \propto A_{ul} g_u / g_l$ and the oscillator strengths, summed over the two transitions, is $f_{2s \rightarrow 3p} = 0.4360$.

¹² The tables for the effective area for FUV and NUV detectors were obtained from https://asd.gsfc.nasa.gov/archive/galex/tools/Resolution_Response/index.html

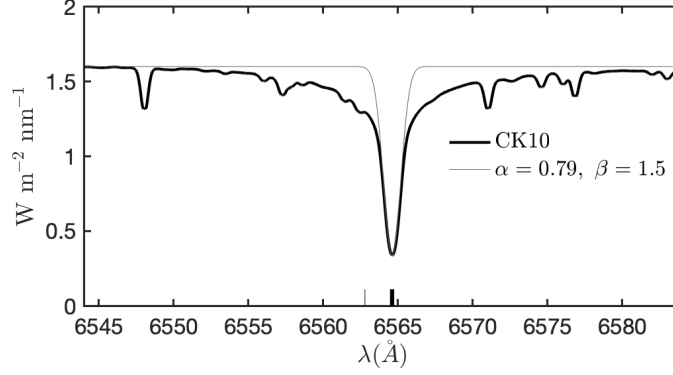


Figure 11. High-resolution spectrum of the Sun in the vicinity of $H\alpha$ (data from [Chance & Kurucz 2010](#)). The absolute level at 6500 Å agrees to within a percent of the spectrum from SOLSPEC, aboard the International Space Station ([Meftah et al. 2021](#)). The dotted curve is a “chi-by-eye” fit restricted to the narrow $H\alpha$ core. The model is given by $y(\lambda) = 1.6 \times [1 - \alpha \exp(-\beta x^2)]$ where $x = \lambda - \lambda(H\alpha)$, $\alpha = 0.79$ and $\beta = 1.5 \text{ \AA}^{-2}$. The thick vertical stub is the vacuum wavelength, $\lambda(H\alpha) = 6564.614 \text{ \AA}$. The thin stub is the rest air wavelength of $H\alpha$ (6562.801 Å), shown merely for reference.

The thermal velocity dispersion of H atoms is $\sigma_v = \sqrt{kT/m_H}$ or 2.9 km s^{-1} for $T = 1,000 \text{ K}$; here, m_H is the mass of an H atom. The corresponding FWHM is $\ln(256)^{1/2} \sigma_v \approx 6.8 \text{ km s}^{-1}$. We fit the solar $H\alpha$ absorption feature to a continuum+Gaussian absorption model (Figure 11) and derive an FWHM of $2\sqrt{\ln(2\alpha)/\beta} = 46 \text{ km s}^{-1}$. Since the geo-coronal H atoms have little Doppler shift with respect to the Sun we can assume that the flux of the solar $H\alpha$ line is constant over the thermal frequency spread of an H atom. The $H\alpha$ flux at the bottom of the absorption line is $0.34 \text{ W m}^{-2} \text{ nm}^{-1}$ (Figure 11). This corresponds to $F_\lambda(0) = 1.1 \times 10^{13} \text{ phot cm}^{-2} \text{ s}^{-1} \text{ \AA}^{-1}$ or $F_\nu(0) = 158 \text{ phot cm}^{-2} \text{ s}^{-1} \text{ Hz}^{-1}$. Then the rate of $H\alpha$ pumping, per atom, is

$$\mathcal{R}_{H\alpha} = F_\nu(0) \frac{\pi e^2}{m_e c} f_{2s \rightarrow 3p} \approx 1.8 d_{\text{AU}}^{-2} \text{ atom}^{-1} \text{ s}^{-1} \quad (\text{B4})$$

where d is the distance in AU. A similar exercise, carried out for solar $H\beta$ absorption, yields

$$\mathcal{R}_{H\beta} \approx 0.27 d_{\text{AU}}^{-2} \text{ atom}^{-1} \text{ s}^{-1}. \quad (\text{B5})$$

The reduction is due to a smaller oscillator strength, $f_{2s \rightarrow 4p} = 0.1028$ and a slightly smaller solar spectral flux, $F(0) = 104 \text{ phot cm}^{-2} \text{ s}^{-1} \text{ Hz}^{-1}$.

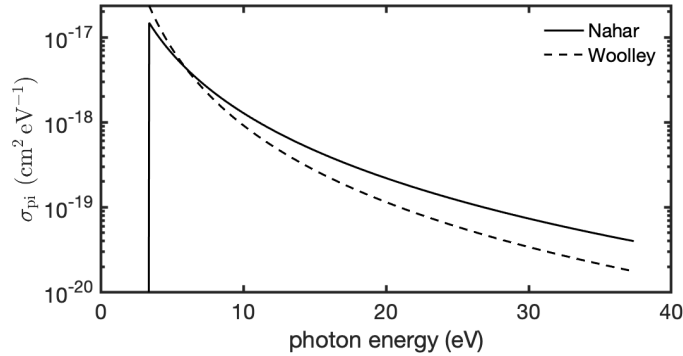


Figure 12. The run of bound-free cross-section as a function of energy of photon (in eV) for the 2s state of hydrogen from [Woolley \(1934\)](#) and [Nahar \(2021\)](#). The cross-section vanishes for photon energy below the ionization edge, $I_H/4$ where I_H is the ionization energy of hydrogen.

Bound-free excitation. The excitation rate from the 2s state¹³ to the continuum is given by $\mathcal{R}_{\text{bf}} = \int_{\nu_\alpha}^{\infty} \sigma_{\text{bf}}(\nu; 2s) F(\nu) / (h\nu) d\nu$ where $F(\nu)$ is the solar spectral flux and $\sigma_{\text{bf}}(\nu; 2s)$ is the bound-free cross-section.

¹³ For 2p levels optical pumping by an external source cannot compete with spontaneous decay to the ground state.

Woolley (1934) offers a simple method to compute this cross-section for $\sigma_{\text{bf}}(\nu; 2s)$. Let f_c be the oscillator strength for this transition. Then $\sigma_{\text{bf}}(\nu; 2s) = (\pi e^2)/(m_e c) f_c \phi_\nu$ where ϕ_ν is the normalized frequency distribution. The bound-free cross-section vanishes for photon energy ($h\nu_0$) below ionization potential from the 2s state, $I_H/4$ where I_H is the ionization potential of hydrogen. It is reasonable to assume that the functional form of the bound-free cross-section is $\propto \nu^{-3}$. The normalization requirement, $\int_{\nu_0}^{\infty} \phi_\nu d\nu = 1$, then yields $\phi_\nu = 2\nu_0^{-1}(\nu/\nu_0)^{-3}$. Next, per the Thomas-Reiche-Kuhn sum rule, $f_c + \sum_{n=3}^{\infty} f(2s \rightarrow np) = 1$; here $f(2s \rightarrow np)$ is the oscillator strength for 2s- np transition. Using the oscillator strengths for the Balmer series¹⁴ we find $f_c = 0.362$. Thus, $\sigma_{\text{bf}}(\nu; 2s) = 1.3 \times 10^{28} \nu^{-3} \text{ cm}^2 \text{ Hz}^{-1}$. Alternatively, we can use modern calculations for $\sigma_{\text{bf}}(\nu)$ (Nahar 2021). The run of $\sigma_{\text{bf}}(\nu)$ with frequency, ν , for the two approaches is shown in Figure 12. The rate of photo-ionization by solar photons from the 2s state, using either formulae, is essentially the same:

$$\mathcal{R}_{\text{bf}} = \int_{\nu_\alpha}^{\infty} \sigma_{\text{bf}}(\nu; 2s) \frac{F(\nu)}{h\nu} d\nu = 0.125 d_{\text{AU}}^{-2} \text{ atom}^{-1} \text{ s}^{-1}. \quad (\text{B6})$$

Here, we used SOLSPEC data for $F(\nu)$ (see Figure 11). Incidentally, the resulting bound-free ionization rate is a tenth of ionization of H atoms by the Lyman continuum photons. The overall rate of solar photonic excitation of 2s state is the sum of the rates given by Equation B4, B5 and and B6, $A_p \approx 2.2 d_{\text{AU}}^{-2} \text{ atom s}^{-1}$. Solar optical pumping reduces the production of two-photon continuum by $A_{2\gamma}/(A_{2\gamma} + A_p)$.

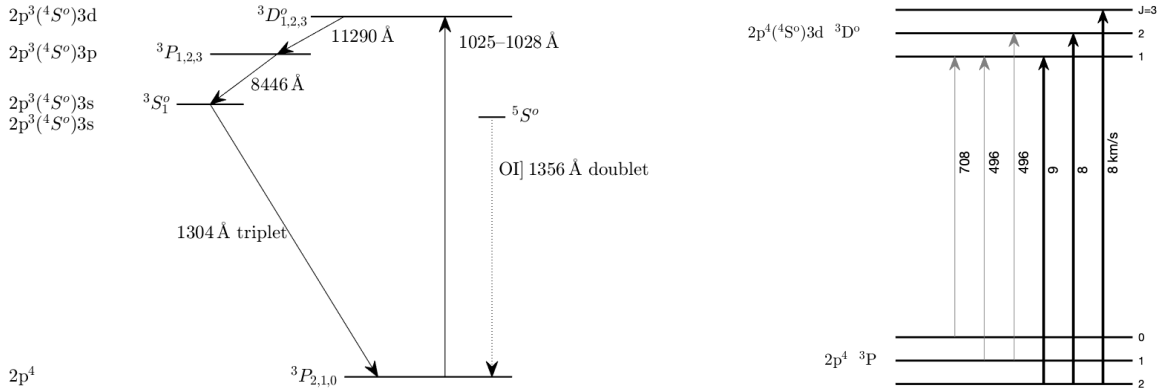


Figure 13. (Left). Partial Grotrian diagram for O I (to scale) displaying key allowed transitions. Solar Ly β photons excite O I atoms from the ground state, $1s^2 2s^2 2p^4 \ ^3P$, to the $1s^2 2s^2 2p^3(4S^o)3d \ ^3D^o$ excited state. The O I atom can decay back to the ground state or decay to the $1s^2 2s^2 2p^3(4S^o)3p \ ^3P$ state which then decays to ground state emitting along the way the famous O I 1304 Å triplet (composed of λ 1302.17 Å, λ 1304.86 Å, λ 1306.03 Å lines). The airglow O I] $\lambda\lambda$ 1355.56 Å, 1358.51 Å is a spin-forbidden ($\Delta S \neq 0$; “inter-combination”, “semi-forbidden”) transition and results from electron excitation of O I from the ground state to the $2p^3(4S^o)3s \ ^5S^o$ level (transition shown by dotted line). (Right): Grotrian diagram of O I (not to scale) restricted to the six allowed transitions between the ground state and $1s^2 2s^2 2p^3(4S^o)3d \ ^3D^o$. The wavelength for each transition is converted to a velocity w.r.t. the rest wavelength of Ly β . The rightmost three lines (thick black color) have sufficiently small velocity shifts, $\approx 9 \text{ km s}^{-1}$, that they can be excited by solar Ly β photons. These three lines are referred to as the “trio” in the main text. The remaining three (gray) lines have large velocity shifts, 500–700 km s^{-1} , and so cannot be excited by solar Ly β .

B.3. Bowen Fluorescence of O I by Ly β

The reason that the measurements in Table 1 are listed as Ly β +OI is because there happens to be a near coincidence between Ly β and an excited state of O I, $1s^2 2s^2 2p^3(4S^o)3d \ ^3D^o$ (Meier et al. 1987; see Figure 13 for a partial Grotrian diagram of O I). The oscillator strengths for all the transitions can be found from the NIST database. The excited OI atom has a probability of 71% to return to the ground state and 29% probability of decaying to the $1s^2 2s^2 2p^3(4S^o)3p \ ^3P$ state with subsequent cascade to ground state with the last lap involving the famous O I λ 1304 Å triplet. In addition to this channel, oxygen atoms in the thermosphere are directly excited by the solar chromospheric O I λ 1304 Å triplet (in emission). Together, these two processes account for the brilliance of the airglow O I triplet. In contrast, the

¹⁴ At little peril, we ignore two-photon decay.

other FUV line of oxygen, O I] $\lambda\lambda 1356, 1358 \text{ \AA}$, is weaker because it is spin-forbidden and is primarily excited by collisions with electrons. For satellites in LEO, such as HST, even in Earth’s shadow, the airglow is dominated by Ly α (2 kilo-Rayleigh or 2 kR), the O I $\lambda\lambda 1302 \text{ \AA}$ triplet (1 kR) and the semi-forbidden O I] $\lambda\lambda 1356 \text{ \AA}$ doublet (0.1 kR). *GALEX*, like HST, was in LEO. The FUV band of *GALEX* was carefully chosen to exclude Ly α and the strong O I triplet and attenuate the semi-forbidden O I] line (Martin et al. 2005).

C. THE THERMOSPHERE

The troposphere (0–12 km) contains most of the atmosphere. The temperature within the stratosphere (12–50 km) increases with height owing to absorption of solar UV by ozone. Once the ozone is dissociated temperature starts to decrease again with height until dissociation of oxygen and other molecules begins in the thermosphere. The mesosphere (50–85 km) is the layer between the stratosphere and the thermosphere. It is in this layer in which meteors burn, providing a convenient layer of Na I for laser guide-star adaptive astronomy.

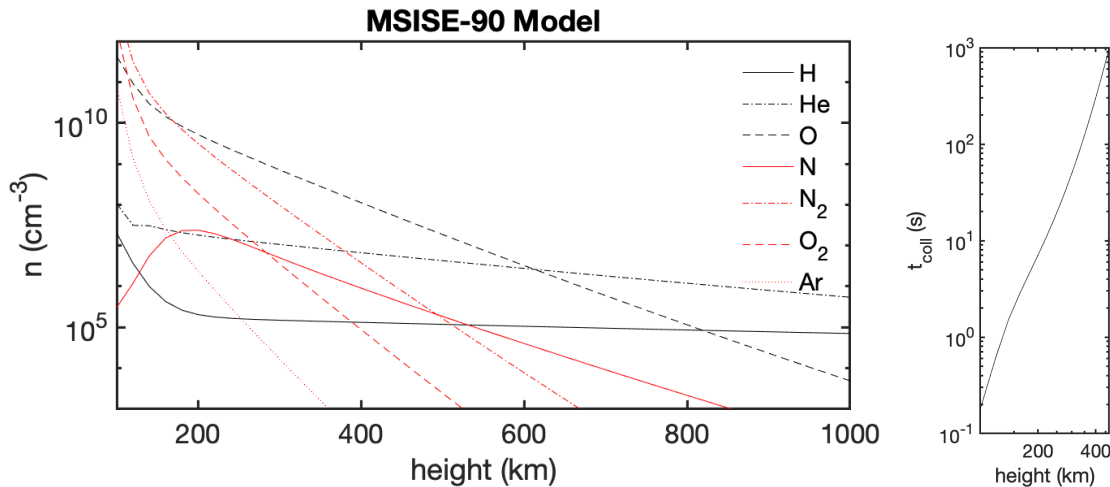


Figure 14. (Left) MSIS-E-90 atmosphere model for latitude of 30° and longitude of 0° on 01-January-2000 at a local time of 0100. From https://ccmc.gsfc.nasa.gov/modelweb/models/msis_vitmo.php (Right). The run, with height, of the mean time between collisions between an H atom and a neutral atom, $\tau = (\sigma_0 \sum_i n_i v_i)^{-1}$ where $\sigma_0 = 10^{-16} \text{ cm}^2$ is the characteristic “hard sphere” approximation for the cross section and n_i is the number density of species i and $v_i = \sqrt{3kT/m_H}$ is the relative velocity between H atom and species i .

The thermosphere (80 to about 700 km) is the region in which low-earth satellites are located (e.g., International Space Station: 420 km; HST 540 km; Swift Observatory: 550 km; *GALEX*: 685 km; FUSE, 750 km). The temperature in the thermosphere increases with height, owing to the absorption of solar EUV radiation by majority molecular species. Thus atoms are the primary constituents of the thermosphere. The temperature is strongly dependent on the solar EUV irradiance, ranging from 800 K to 2000 K (with strong day/night dependence). The radial extent of the thermosphere is quite sensitive to solar EUV, puffing up to 1000 km during solar maximum and receding to 500 km during solar minimum.

The density, ionization fraction and temperature of the thermosphere were obtained from the Community Coordinating Modeling Center (CCMC) portal¹⁵: MSIS-E-90 (“Mass Spectrometer and Incoherent Scatter radar - Exosphere-[19]90”) for the run of neutral particles (Figure 14) and IRI-2016 (International Reference Ionosphere – 2016). Hydrogen is a minority species in the thermosphere and, furthermore, suffers from outflow. As such, Bishop et al. (2001) argue that the hydrogen density profile in MSIS is not reliable.

D. THE IONOSPHERE

As can be seen from Figure 15 the IRI-2016 model for electrons stops at 2,000 km. The higher altitude profile was generated, at my request, by Matthew Zettergren, Embry-Riddle Aeronautical University. The GEMINI open-source

¹⁵ <https://ccmc.gsfc.nasa.gov/about.php>

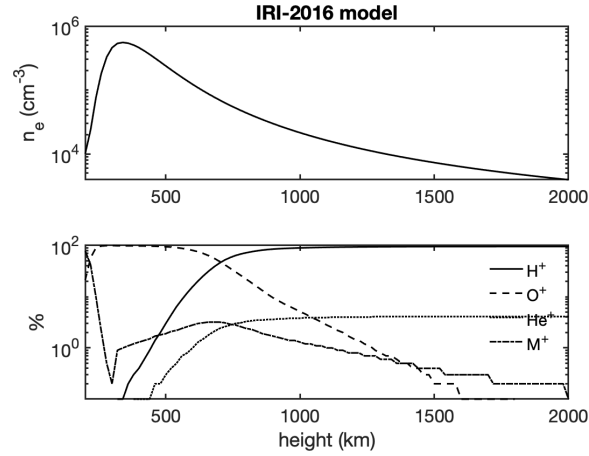


Figure 15. (Top) The run of electrons with altitude. (Bottom) The run of H^+ , He^+ , O^+ and other ions (“ M^+ ”: O_2^+ , N^+ and NO^+), but expressed as a percentage of the electron density.

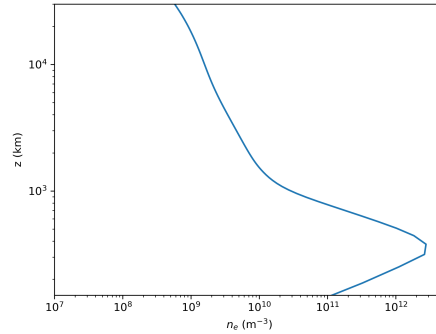


Figure 16. Radial profile of electrons (equatorial plane). Note the unit for electron density is m^{-3} . Figure supplied by Matthew D. Zettergren.

ionospheric model¹⁶ was used in a 2-D meridional, dipole configuration to simulate plasma density evolution over several days (e.g., Zettergren & Snively 2015). The grid used covers $\pm 60^\circ$ in latitude, corresponding to apex altitudes of about 32,000 km (altitude of the model grid above magnetic equator). GEMINI solves conservation of mass, momentum, and energy equations for the ionospheric plasma for 6 ion species relevant to the terrestrial ionosphere, including protons. The model was run moderate for high solar and geomagnetic activity levels of $\text{F10.7}=129.5$, $\text{F10.7a}=104.7$, and solar index $\text{Ap}=37$. The date of the simulation is 10/6/2011 (near equinox) and the UT is about 5:45 (corresponding roughly to noon local time), representing a typical daytime plasma density state. Figure 16 shows a profile extracted from the geomagnetic equator. The results are meant to be illustrative of plasmasphere conditions during geomagnetically quiet times.

E. THE EXOSPHERE

The exosphere is defined as the region in which the collisions of neutral particles with each other ceases to be important. The base of the exosphere (“exobase”) depends on solar activity but a typical value is 500 km. Three families of particles are defined as follows: “ballistic” – particles that lack sufficient speed and so fall back; “escapers” – particles which have sufficient speed to escape; and “satellite” — particles which undergo a rare collision ($R \lesssim 2.5 R_E$) which sends them back down. Thus the particle density of the exosphere is not a simple power law. The temperature in the exosphere decreases to one third of the base value at $4 R_E$ and two-fifth at $10 R_E$; here, R_E is the radius of Earth ($\approx 6,400$ km). We adopt the “standard” temperature of 1025 K (cf. Østgaard et al. 2003). The corresponding thermal rms velocity is 2.9 km s^{-1} .

¹⁶ <https://github.com/gemini3d>

F. STP 78-1 & MINISAT-01

The Space Test Program 78-1 (STP 78-1; aka “Solwind”)¹⁷ was launched in 1979 into a sun-synchronous orbit (600 km height). The satellite spin-orbital axis was perpendicular to the Earth-Sun axis (i.e., a “noon-midnight” orbit). It carried, amongst other instruments, an EUV/FUV spectrometer for studies of airglow (Chakrabarti et al. 1984). The spectrometer had an entrance window of $18^\circ \times 9^\circ$ and operated over 350–1400 Å band. Chakrabarti et al. (1984) reported satellite night-time EUV spectrum of airglow, both looking “down” (zenith angle, z , between 120° and 150°) and looking “up” (zenith angle between $30^\circ < z < 80^\circ$).¹⁸ The relevant measurements are summarized in Table 1.

The Spanish Minisat-01 spacecraft (Morales et al. 1998) carried a high spectral resolution EUV spectrometer, EURD (“Espectrógrafo Ultravioleta extremo para la Radiación Difusa”; Edelstein et al. 2006). The orbit was a circle with height of 580 km and inclined 151° with respect to the equator. Observations were obtained only during satellite midnight, specifically restricted to zenith angle of -85° (just before ground dawn)¹⁹ and $+80^\circ$ (just after dusk). Restricting to absolute zenith angle of $< 70^\circ$, $\text{Ly}\beta$ was detected at a level of $6.4 R$ (López-Moreno et al. 2001).

G. SWAN & IMAGE

The Solar & Heliospheric Observatory (SOHO) is a ESA-NASA mission that is located in the vicinity of the Earth-Sun L1 region and focused on the studies of the atmosphere of the Sun, the solar wind and helio-seismology. It carries Solar Wind ANistoropies (SWAN) instrument whose primary goal is to study the structure of the solar wind through its interaction with the IPM. A hydrogen cell acts by absorbing the incident solar light at the rest wavelength of $\text{Ly}\alpha$. In effect, the cell provides a spectral resolution of 10^5 (Bertaux et al. 1995). SWAN data has also been used to study the distribution of geo-coronal H atoms (Baliukin et al. 2019).

IMAGE (Imager for Magnetopause-to-Aurora Global Exploration) was a NASA Medium Explorer class mission that was designed to study the response of Earth’s magnetosphere to changes in the solar wind. It was launched into a highly elliptical orbit (1,000 km \times 46,000 km) with an inclination of 90.01° and an orbital period of about 14 hours. Its payload included an FUV imaging system which included the “GEO” photometer (Mende et al. 2000). The three photometers, oriented differently, respond to radiation coming from within their 1-degree FoV in the wavelength range 1150–1500 Å. This instrument was designed to measure the brightness of the geo-coronal $\text{Ly}\alpha$. ØStgaard et al. (2003) provide a two-exponential model fit to the observed brightness. An example fit is

$$I(r) = 16.9 \exp(-r/1.03) + 1.06 \exp(-r/8.25) \text{ kR} \quad (\text{G7})$$

where $I(r)$ is the $\text{Ly}\alpha$ intensity and the radius r is in units of R_E . Under the (admittedly simplistic) assumption of the medium being optically thin the authors invert the observations and provide density profile for H atoms.

¹⁷ Unfortunately, towards the end of the mission, Solwind was assigned as target for a pilot demonstration of anti-satellite technology (ASAT). On September 13, 1985 the satellite was destroyed by an ASM-135 missile mounted on an F-15 fighter airplane.

¹⁸ We interpret the geometry as follows: the line starting at the Sun, going through Earth and then the satellite defines the axis with which z is measured; thus, $z = 0$ is when the satellite is in the night sky and the Earth is below the satellite.

¹⁹ In contrast to the STP-78 convention the authors appear to have assigned a sign to z depending on whether line-of-sight is towards East or West